ФИЗИКА ЭЛЕМЕНТАРНЫХ ЧАСТИЦ И АТОМНОГО ЯДРА
2006. Т. 37. ВЫП. 2

УДК 539.17

NUCLEAR MULTIFRAGMENTATION AND PHASE TRANSITIONS IN HOT NUCLEI

V. A. Karnaukhov

Joint Institute for Nuclear Research, Dubna

ФИЗИКА ЭЛЕМЕНТАРНЫХ ЧАСТИЦ И АТОМНОГО ЯДРА
2006. Т. 37. ВЫП. 2

УДК 539.17

NUCLEAR MULTIFRAGMENTATION AND PHASE TRANSITIONS IN HOT NUCLEI

V. A. Karnaukhov

Joint Institute for Nuclear Research, Dubna

The nuclear multifragmentation is a new, multibody decay mode of very hot nuclei. The measured key properties of this process are considered such as the space-time and temperature characteristics. The experimental data on the critical temperature for the nuclear liquid–gas phase transition are analyzed. Thermal multifragmentation is interpreted as the result of spinodal decomposition, which is acctually the specific nuclear liquid–fog phase transition of first order.

Ядерная мультифрагментация является новым многотельным типом распада очень горячих ядер. Рассмотрены такие ключевые характеристики этого процесса, как пространственно-временные и температурные. Проанализированы экспериментальные данные о критической температуре для ядерного фазового перехода жидкость–газ. Тепловая мультифрагментация интерпретируется как результат развала горячего ядра в спинодальной области, который следует рассматривать как специфически ядерный фазовый переход первого рода жидкость–туман.

INTRODUCTION

Nuclear fragmentation was discovered almost 70 years ago [1, 2] in the cosmic-rays studies as a puzzling phenomenon accompanying collisions of relativistic protons with a target and consisted in emission of slow nuclear fragments. Their masses were heavier than those of alpha particles, but lighter than those of fission fragments. Now they are called as intermediate mass fragments (IMF, $3 \leqslant Z \leqslant 20$). Later on (in the 1950s), this phenomenon was observed in the experiments at the accelerators by Perfilov, Lozkin et al. [3, 4]. The multiple fragment emission was also observed in these earlier studies, when nuclear emulsion had been irradiated by 9 GeV protons at the Dubna Synchrophasotron (multifragmentation?). Mechanism of this process was unclear and it was investigated leisurely for three decades. The situation changed dramatically after 1982, when Jakobsson et al. observed a multiple emission of IMFs in emulsion irradiated by the carbon beam of 250 MeV/nucleon at the Berkeley Bevalac [5]. This observation was done at the time, when the phase transitions in hot nuclear media became of the great interest. The experimental data on fragmentation stimulated appearance of a number of theoretical models, which related the copious production of IMF to the liquid–gas phase transition in nuclear matter. In a nucleus, as in usual liquid, peculiar conditions can be created (high temperature and reduced density),

when system enters the region of phase instability (spinodal region). This state may disintegrate into an ensemble of small droplets (IMFs), surrounded by a nuclear gas (nucleons and light composite particles with $Z \leqslant 2$). This scenario of multifragmentation (spinodal decomposition) was discussed first in 1983 by Siemens [6].

The idea of getting a new insight into the problem of the nuclear equation of state stimulated great interest in the multifragmentation phenomenon in the middle of the 1980s. A number of very informative studies were performed in the inclusive approach (e.g., see the papers by Purdue University group [7, 8] and Dubna group [9]). At that time, a dozen very complicated 4π-devices were created to study this process with heavy ion beams, which are well suited for producing extremely hot nuclei. But in this case heating of nuclei is accompanied by compression, strong rotation and shape distortion, which can essentially influence the decay properties of excited nuclei. Investigation of dynamic effects caused by excitation of collective (or «mechanical») degrees of freedom is interesting in itself, but there is a great problem of disentangling all these effects to get information on the thermodynamic properties of a hot nuclear system. One gains simplicity, and picture becomes clearer, when light relativistic projectiles (first of all, protons, antiprotons, pions) are used. In contrast to heavy ion collisions, fragments are emitted by only one source — the slowly moving target spectator. Its excitation energy is almost entirely thermal. Light relativistic projectiles provide therefore a unique possibility of investigating «thermal multifragmentation», the process which is governed by heating of nucleus. Figure 1 [10] illustrates the central collision of a relativistic proton with a heavy target. Passing through the target, the proton creates an intranuclear cascade. Fast cascade particles are ejected into the forward hemisphere, but slower ones are absorbed by the target spectator. The hot remnant nucleus expands and disintegrates by emitting nucleons and fragments.

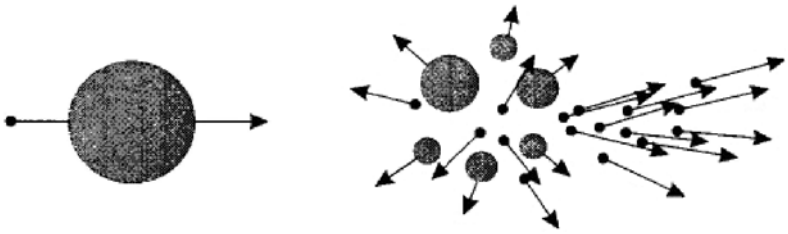

Fig. 1. Picture of collision of a swift proton with a heavy nucleus [10]

The interplay of thermal and collective excitations in the process of copious IMF emission was considered in a number of studies (e.g., [11]). Figure 2 shows the diagram computed in [11] with the hydrodynamic approach and the

percolation model. The IMF emission was considered for heated and compressed ^{208}Pb nucleus. The left lower sector of the diagram is a domain of ordinary particle evaporation, true multifragmentation (many-body decay) occurs above the line. Compression is as effective for multifragmentation as thermal excitation. Even the cold nucleus can disintegrate when the compression energy is larger than 3.5 MeV/nucleon. The influence of rotation and shape distortion on the multifragmentation probability was analyzed in several papers (e.g., [13]). But compression is expected to be a more important dynamic property of heavy ion collisions in that aspect. The reactions induced by relativistic light projectiles occupy only abscissa area since $E^*/A \cong \varepsilon_t$, the domain of heavy ion collisions is entire area of the diagram because, in that case, the excitation energy is composed by the thermal and compression terms: $E^*/A = \varepsilon_t + \varepsilon_c$. In fact, the threshold for thermal multifragmentation is slightly lower than predicted in [11] (solid point in Fig. 2 [12]): the actual border between the evaporation and multifragmentation regions is given by the dashed line. There are a number of review papers in the field, e.g., [14–26].

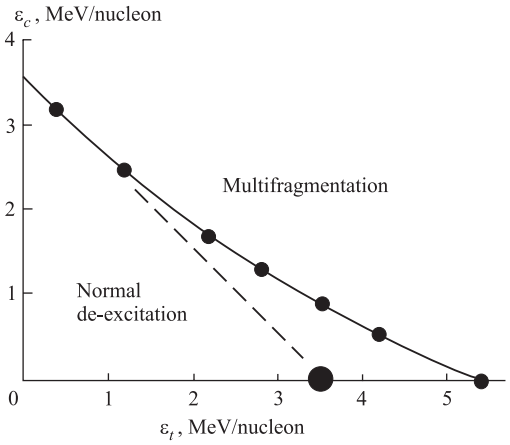

Fig. 2. Multifragmentation and ordinary de-excitation regions calculated for ^{208}Pb as a function of the thermal and compression energies per nucleon [11]. The large symbol at abscissa shows the experimentally estimated threshold for the thermal multifragmentation of target spectator for $p + \mathrm{Au}$ collisions [12]

A vast body of data accumulated so far provides the possibility of thoroughly analyzing the thermal and dynamical multifragmentation processes with the aim of revealing their common and distinguishing feature. This is done in the next Section considering the data on the mean IMF multiplicities, the fragment charge distributions, kinetic energy spectra, and the time scale of IMF emission. In both cases it is proved that multifragmentation is the main decay mode for nuclei with excitation energy above the threshold of this decay channel. The statistical models are very successful in describing the properties of thermal multifragmentation. But they fail to treat fragment emission in central nucleus–nucleus collisions when the compression is decisive for nucleus disintegration. We follow our paper [27]

in this analysis. After that we concentrate on the thermal multifragmentation to make an emphasis on the relation of this phenomenon and phase transitions in hot nuclei.

1. FRAGMENTATION INDUCED BY LIGHT RELATIVISTIC PROJECTILES AND HEAVY IONS: SIMILARITIES AND DIFFERENCES

1.1. IMF Multiplicity. In this paper we define $\langle M \rangle$ as a mean IMF multiplicity for the events with emission of at least one IMF. The mean fragment multiplicity averaged over all inelastic collisions $\langle M^* \rangle$ is connected with $\langle M \rangle$ via the relation $\langle M^* \rangle = \langle M \rangle [1 - P(0)]$, where $P(0)$ is the probability of the events without IMF emission. Thus $\langle M \rangle$ is never smaller than one.

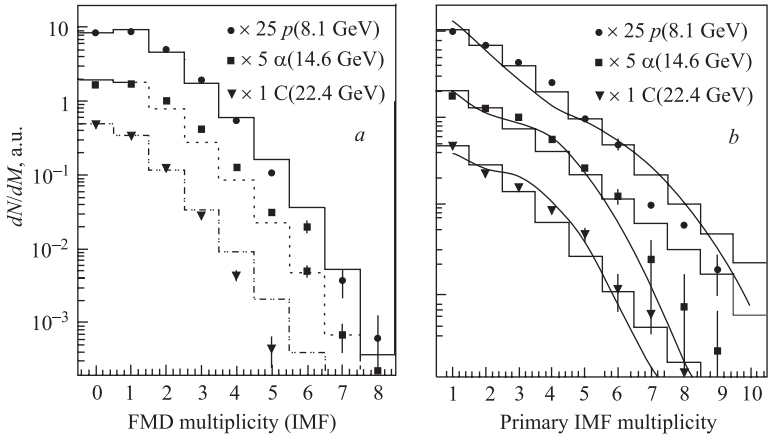

Fig. 3. *a*) Measured IMF-multiplicity distributions and fits with Fermi functions for $p + \mathrm{Au}$ collisions at 8.1 GeV, $^4\mathrm{He} + \mathrm{Au}$ at 14.6 GeV, and $^{12}\mathrm{C} + \mathrm{Au}$ at 22.4 GeV [28]; *b*) the symbols represent directly reconstructed primary IMF distributions, the lines are calculated with the INC + Expansion + SMM model

Figure 3 shows examples of inclusive IMF-multiplicity distributions observed in collisions of relativistic light projectiles (8.1 GeV protons, 14.6 GeV ^{4}He and 22.4 GeV ^{12}C) with gold target [28, 29]. Experimental data (Fig. 3, *a*) have been obtained using 4π-device FASA installed at the external beam of the Dubna Synchrophasotron [30, 31]. At present, this setup consists of five ΔE–E telescopes surrounded by fragment multiplicity detector (FMD), which is composed of 64 scintillation counters with thin CsI(Tl). The primary multiplicity distributions (Fig. 3, *b*) have been reconstructed from the data taking into account the experimental filter. The mean inclusive multiplicity was found to be $\langle M \rangle \approx 2$ indicating

the so-called limiting fragmentation, which is caused by a saturation of the excitation energy of the target spectators. Note that the distributions are rather wide reaching the multiplicity values 8–9. More than 30% of events are characterized by $M \geqslant 3$. The multiplicity distributions are well described by combined model denoted as INC + Expansion + SMM. The model works satisfactorily for all the reactions presented in Fig. 3.

Let's consider in few words this model. The reaction mechanism for the light relativistic projectiles is usually divided into two steps. The first one is a fast energy deposition stage, during which energetic light particles are emitted and the nuclear remnant is excited. The fast stage is usually described by the intranuclear cascade model (INC). We use the version of the INC from [32, 33] to get the distribution of the nuclear remnants in charge, mass and excitation energy. The second stage is described by the Moscow–Copenhagen statistical multifragmentation model (SMM) [19, 34, 35]. Within the SMM the probability of different decay channels of the excited remnant is proportional to their statistical weights. The volume of the system at the stage of fragment formation is taken to be $V_t = (1 + k)A_{\mathrm{MF}}/\rho_0$, where A_{MF} is the mass number of the decaying nucleus, ρ_0 is the normal nuclear density, k is the model parameter. Usually this parameter is taken to be $k \approx 2$. Thus, thermal expansion before the break-up is assumed. The «partition» density is $\rho_t = \rho_0/(1 + k)$. It is found that this traditional approach fails to describe the observed IMF multiplicities overestimating the mean IMF multiplicities. Expansion stage is inserted between the two parts of the calculations. This is done in spirit of the Expanding Emitting Source model, EES [41], which considers the particle evaporation during the expansion. According to the recipe of [12, 28, 29], the excitation energies and the residual masses are empirically tuned to get agreement with the measured IMF multiplicities, i.e., the values for the residual (after INC) masses and their excitation energies are scaled on an event-by-event basis. Other well-known statistical models of multifragmentation are presented in the papers [36–40].

We shall discuss especially in Subsec. 2.2 the size parameters of multifragmentation. It will be shown in contrast to traditional assumption of SMM, that there are *two* characteristic volumes (or densities) for this process. The first, V_t, corresponds to the configuration of the system at the stage of prefragment formation, transition state configuration. The second one, V_f, is the freeze-out volume, when fragments are separated so that they interact only via the Coulomb force. The second volume is larger than the first one. The final part of the SMM is a calculation of the multibody Coulomb trajectories, which starts with placing all of the charged particles of a given partition inside the freeze-out volume. Each particle is assigned a thermal momentum corresponding to the system temperature for a given final channel.

Figure 4 displays a sample of data on specific mean IMF multiplicity per nucleon, $\langle M \rangle / A$, for collisions $a + \mathrm{Au}$. Projectile a ranges from relativistic

protons, ^{3,4}He [12, 42, 43] to heavy ions like ^{197}Au [44, 45]. The data are shown as a function of the incident energy in the centre-of-mass system. There are no definite experimental data on the mass numbers of fragmenting nuclei except for peripheral $\mathrm{Au} + \mathrm{Au}$ collisions at 600 MeV/nucleon (the last point along energy scale in Fig. 4) [19]. For the proton-induced fragmentation at beam energies of 2.16, 3.6, and 8.1 GeV, source mass numbers A were obtained from the fit of data to the calculations within the combined model described above. For ^{40}Ar [46], ^{36}Ar [47], ^{129}Xe [48] beams, the mass numbers of source were estimated under the assumption of the same mass loss with respect to the initial system as in the case of the proton-induced fragmentation (at the closest energy). For $\mathrm{Au} + {}^{12}\mathrm{C}$ collisions the A value was found by a procedure similar to that used for the peripheral $\mathrm{Au} + \mathrm{Au}$ collisions, since the spectator fragmentation at relativistic and subrelativistic bombarding energies is thought to be universal [44]. The symbols in Fig. 4 represent the inclusive data (averaged over the entire range of the impact parameters) except the open circle which corresponds to the central $\mathrm{Au} + \mathrm{Au}$ collisions at 100 MeV/nucleon [45].

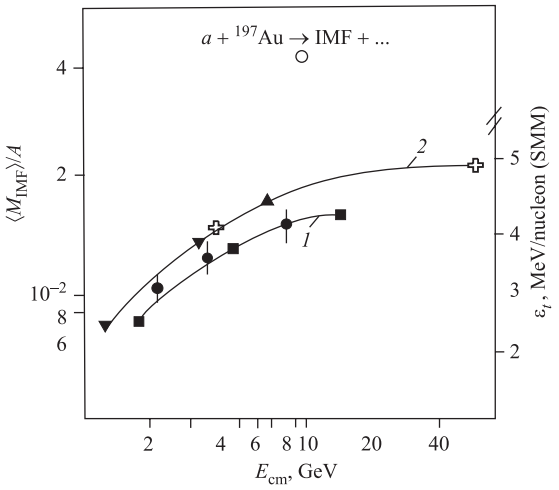

Fig. 4. Specific IMF multiplicity for $a + {}^{197}\mathrm{Au}$ collisions as a function of c.m. energy of the system. *1*: circles — for relativistic proton beam; squares — for ^{3}He and ^{4}He beams. *2* is for heavy ion beams: ^{40}Ar, ^{36}Ar, ^{129}Xe, ^{12}C (inverse kinematics), and ^{197}Au. Open circle is for the central $\mathrm{Au} + \mathrm{Au}$ collisions, others symbols are the inclusive data. The right scale gives the excitation energy per nucleon according to SMM

The inclusive specific IMF multiplicities for the peripheral heavy ion collisions are only slightly larger than those for the fragmentation induced by relativistic light projectiles. The process is almost insensitive to reaction dynamics. This observation suggests that the energy transfer to the residual nucleus is the primary quantity controlling its decay. On the right scale of Fig. 4 the excitation energy per nucleon is plotted according to SMM. This is the thermal excitation energy, which is slightly larger for heavy ion reaction than for target spectators produced by relativistic protons and He ions.

The situation is different for the central collisions of very heavy ions, which are characterized by large contribution of the collective (compression) term into the system excitation energy. Figure 5 shows the IMF-multiplicity distributions measured for $\mathrm{Au} + \mathrm{Au}$ collisions at 200 MeV/nucleon. It was done in 1987 [49] by the group headed by A. M. Poskanzer with Plastic Ball/Wall system at the Bevalac (Berkeley). This electronic setup was the first 4π-device, which could be used for the multifragmentation study. The Plastic Ball includes 815 detector modules, which represent a particle identifying telescopes with ΔE and E detectors using a slow and fast scintillator read-out via one photomultiplier [50]. The angular acceptance of Plastic Ball/Wall system for light charged particles is close to 4π allowing each event to be characterized by the total charged particle multiplicity M_{cp}. The last is directly related to the impact parameter of collision. Fragment multiplicity distributions in Fig. 5 are given for five bins of M_{cp}, corresponding to $0 < M_{\mathrm{cp}} \leqslant 23$, $23 < M_{\mathrm{cp}} \leqslant 46$, $46 < M_{\mathrm{cp}} \leqslant 69$, $69 < M_{\mathrm{cp}} \leqslant 92$, $M_{\mathrm{cp}} > 92$. The first bin corresponds to the peripheral collisions with rather low excitation energy of remnant, which emit less than one IMF per event. The last bin corresponds to the most central collisions, for which the IMF-multiplicity distribution has a maximum at $M \approx 4$. Note that these measurements are performed at the laboratory angles $\theta_{\mathrm{lab}} < 30^{\circ}$, corresponding to the forward hemisphere in the center of mass. Extrapolation of this measurement to 4π leads to 8 or more intermediate mass fragments per events in central collisions, with significant number of the events producing as many as 20 fragments.

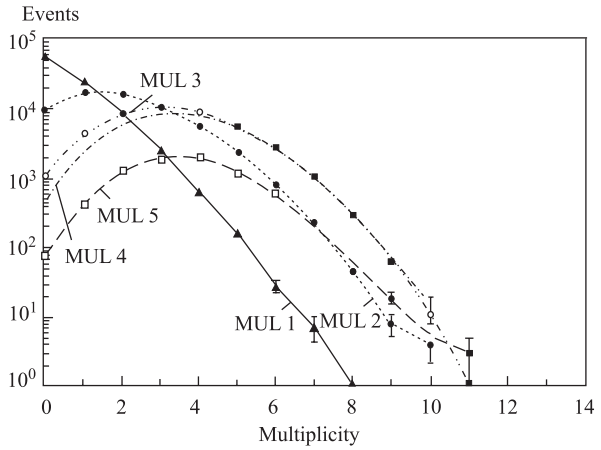

Fig. 5. Multiplicity distributions of fragments created in $\mathrm{Au} + \mathrm{Au}$ collisions at 200 MeV/nucleon and measured by Plastic Ball/Wall (Berkeley). Data are given for five total charge multiplicity bins from MUL1 (peripheral) to MUL5 (most central collisions) [49]

These observations were confirmed in later sophisticated studies by FOPI collaboration at GSI (Darmstadt) [51]. The detector FOPI, installed at SIS-GSI (Darmstadt), was built in two phases: Phase I, covering the forward hemisphere (in c.m. system) and based on time-of-flight plus energy-loss methods to identify and characterize the emitting particles, and Phase II, which extended the detector to 4π geometry and added magnetic analysis. It was found in these studies that the statistical models fail to describe the data for the most violent collisions of heavy ions, when approximately 60% of the available energy is stored into radial flow produced by the compression of the system at the early stage of collision. The most impressive manifestation of the collective flow is seen in fragment kinetic energy spectra considered in the next section.

1.2. Fragment Kinetic Energy Spectra. In Fig. 6, the energy spectrum of fragments from purely thermal multifragmentation is exemplified by the carbon spectrum from $p + \mathrm{Au}$ collisions at 8.1 GeV [27]. The curve represents the result of calculations based on the combined ($\mathrm{INC} + \mathrm{Exp.} + \mathrm{SMM}$) model. It is shown in [52] that about 75% of the mean energy of carbon fragments are gained from the Coulomb acceleration, and only a quarter is purely thermal contribution. Therefore, the mean fragment energy is sensitive to the size of the source (Z, A, and R). Some very important details concerning the size parameters of multifragmentation and the statistical model of the process will be discussed in the next Section. The model considers the break-up of the hot expanded system under assumption that the expansion velocity equals zero. Agreement between the data and the calculated curve is rather good and the upper limit of the expansion velocity at the break-up moment is less than 0.02 c, which corresponds to the mean flow energy less than 0.2 MeV/nucleon.

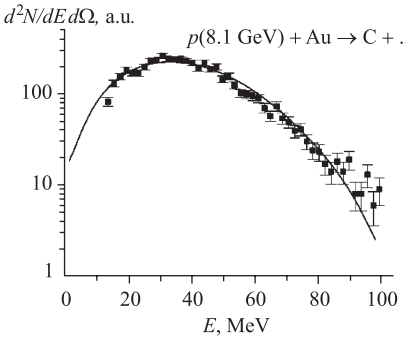

Fig. 6. Energy spectrum of carbon from $p +$ Au collisions at 8.1 GeV, along with the results of the model calculation

The situation is changed with increasing the projectile mass because of onset of the collective flow. It is illustrated by Fig. 7, which presents the data sample for the mean IMF energies per nucleon for collisions of various projectiles with a gold target: protons, ^{4}He [29], ^{36}Ar [53], for peripheral collisions of Au projectiles [44] and for central collisions of Au projectiles [45, 54]. For proton and ^{4}He beams the direct measurements were used for $\theta = 87^\circ$ with respect to the beam direction. For ^{36}Ar, data were obtained from the measured transverse energy of the fragments. For the projectile-spectator fragmentation in peripheral

$\mathrm{Au} + \mathrm{Au}$ collisions, energies are estimated from the width of the transverse and longitudinal momentum distributions of IMF. For central $\mathrm{Au} + \mathrm{Au}$ collisions, the direct measurements of fragment energies and times of flight are used.

For heavier than proton projectiles, the mean IMF energies are higher (even for ^{4}He beam) than those for the proton-induced collisions. They are dramatically higher for the central $\mathrm{Au} + \mathrm{Au}$ collisions and that cannot be caused by the larger source charge Z_s. It is estimated to be around 120 for the incident energy of 100 MeV/nucleon [45] and this can account for only a part of the increase in the IMF energies. By and large, this is explained by the effect of the radial flow initiated by significant compression of nuclear matter in a collision process. For an incident energy of 150 MeV/nucleon of the Au beam the flow energy is found to be equal to 19.9 ± 0.3 MeV/nucleon. This value was obtained from the analysis on the basis of the «blast model», which describes well the IMF energy spectra for central collisions at 150–400 MeV/nucleon [51].

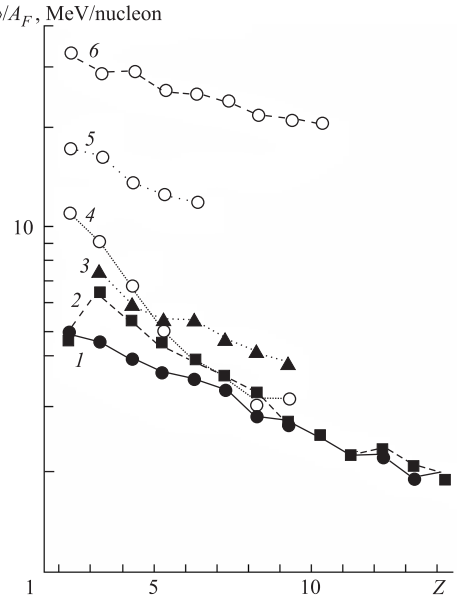

Fig. 7. IMF mean energies per nucleon as a function of charge for collisions of various projectiles with gold target: *1* — for p beam at 8.1 GeV; *2* — ^{4}He projectiles at 3.65 GeV/nucleon; *3* — ^{36}Ar, 110 MeV/nucleon; *4* — ^{197}Au, 600 MeV/nucleon, peripheral collisions; *5*, *6* — central collisions of $\mathrm{Au} + \mathrm{Au}$ at 100 and 150 MeV/nucleon, respectively

According to this analysis, around 60% of the available energy is stored in the radial flow. A minor enhancement of the IMF mean energies in ^{4}He- and ^{36}Ar-induced fragmentation in relation to that for $p + \mathrm{Au}$ interaction can also be attributed to the effect of a collective flow which just comes to the game.

In case of peripheral $\mathrm{Au} + \mathrm{Au}$ collisions (curve *4*), there arises the problem of estimating the contribution of the Coulomb field of the target spectator to the kinetic energy of the fragment originating from the projectile spectator. The typical time for thermally driven expansion of the system before the break-up is estimated to be around 50–70 fm/c [12]. The space separation of the target and projectile spectators is ≈ 50 fm after that time. At this distance, the Coulomb field

of the target is greatly reduced. It cannot affect significantly the kinetic energy of the fragments if they are emitted after the expansion time. A comparison of curves *4* and *2* in Fig. 7 shows that the energies of fragments with $Z > 4$ for $\mathrm{Au} + \mathrm{Au}$ collisions are close to that from $^4\mathrm{He} + \mathrm{Au}$ collisions. But fragment energies for $Z = 2$ and 3 are noticeably greater in the first case. In Ref. [27], it is suggested that the light fragments are emitted at least partly before the expansion, when the Coulomb field of the target is still significant.

1.3. Fragment Mass (Charge) Distributions. Figure 8 gives an example of mass distributions for the thermal multifragmentation induced in gold by relativistic alpha projectiles [55]. Mass spectra were measured in the time-of-flight telescopes of FASA setup [30] as a function of the multiplicity of LCP's given by the fragment multiplicity detector. For the low LCP multiplicity the mass distribution shows two contributions: one of heavy fragments in the mass region around $A = 80$, most likely fission fragments. This contribution disappears rapidly with increasing LCP multiplicity, reflecting increasing of the excitation energy. The second, lighter-mass component, is seen at all the chosen multiplicities. The mass

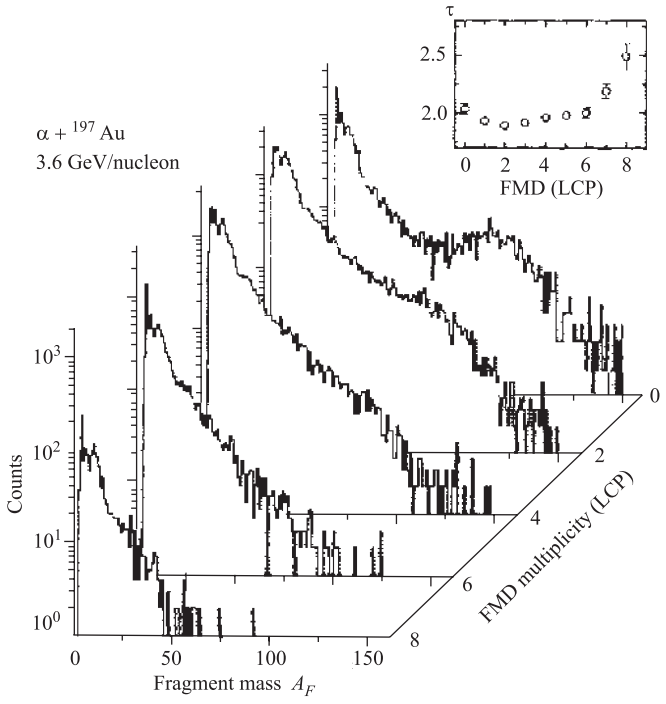

Fig. 8. Mass spectra for $^4\mathrm{He}(14.6\ \mathrm{GeV}) + \mathrm{Au}$ collisions measured in the time-of-flight telescopes of FASA setup as a function of the LCP multiplicity. The insert gives the τ, power-law parameter, deduced from the mass spectra in the region $10 \leqslant A \leqslant 40$

yield in the range $10 \leqslant A \leqslant 40$ is well described with the power-law, $A^{-\tau}$. The exponent τ is given in the insert of Fig. 8 as a function of the LCP multiplicity (not corrected for the efficiency). A minimum is observed at the measured multiplicities of 2–4 light charged particles (correction for the detection efficiency is not done).

Such a minimum of τ parameter has been reported earlier by the ALADIN collaboration for fragmentation induced in various targets by Au projectiles at a bombarding energy of 600 MeV/nucleon [56]. The experiment was performed with ALADIN forward spectrometer [57]. Projectile fragments are tracked and identified in the time-projection chamber MUSIC and in the time-of-flight wall. A 64-element Si-CsI hodoscope measured the multiplicity of light charged particles. This was used to calculate the excitation energy deposited in the projectile spectator. It was found that with increasing violence of the collision, the mean multiplicity of intermediate mass fragments first increases to maximum $\langle M_{\mathrm{IMF}} \rangle \approx 3$ (corresponding to the minimum value of the power-law exponent) and then decreases. This is the so-called rise and fall effect in multifragmentation, which is in accordance with the statistical model prediction [19]. Note that the observation of minimum for the power-law exponent (Fig. 8) gives the evidence that the region of maximum of IMF multiplicity can be reached with relativistic light projectiles.

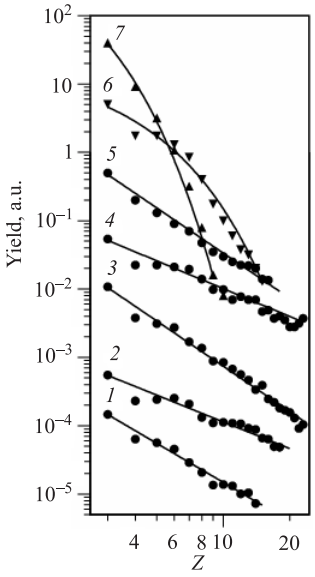

Fig. 9. IMF charge distributions from $a + {}^{197}\mathrm{Au}$ collisions. Projectiles: *1* — p (8.1 GeV); *2* — ${}^{40}\mathrm{Ar}$ (30 MeV/nucleon); *3* — ${}^{84}\mathrm{Kr}$ (35 MeV/nucleon); *4* — ${}^{40}\mathrm{Ar}$ (220 MeV/nucleon); *5* — ${}^{197}\mathrm{Au}$ (1000 MeV/nucleon, peripheral collisions); *6* — ${}^{197}\mathrm{Au}$ (100 MeV/nucleon, central collisions); *7* — ${}^{197}\mathrm{Au}$ (400 MeV/nucleon, central collisions)

A sample of data on the charge distributions for fragments produced in the collisions of various projectiles with the gold target is given in Fig. 9. Distributions *1–4* are inclusive, obtained with the beams of protons (8.1 GeV) [12], ${}^{40}\mathrm{Ar}$

(30 and 220 MeV/nucleon) [58] and ^{84}Kr (35 MeV/nucleon) [59]. Distribution *5* is measured for the peripheral $\mathrm{Au} + \mathrm{Au}$ collisions at 1000 MeV/nucleon [45]. All these distributions can be closely approximated by the power-law dependence. This similarity is remarkable.

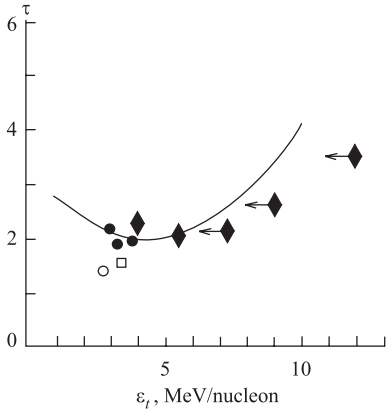

Fig. 10. Power-law parameter τ as a function of the excitation energy. The line is calculated with SMM. Experimental data: solid dots are for $p + \mathrm{Au}$ collisions at 2.16, 3.6, and 8.1 GeV; diamonds are for peripheral $\mathrm{Au} + \mathrm{Au}$ collisions at 600 MeV/nucleon (selected by impact parameter); open symbols are for beams of ^{40}Ar (30 MeV/nucleon) and ^{84}Kr (35 MeV/nucleon)

To discuss the ability of the statistical multifragmentation model to fit the data, let us consider Fig. 10, which presents the comparison of the measured values for the exponent τ with the ones calculated by SMM as a function of the excitation (thermal) energy per nucleon. In these calculations Z, A, and E^*/A of the system were generated by the INC code for the $^4\mathrm{He} + \mathrm{Au}$ collisions at 3.65 GeV/nucleon. For the excitation energies below 10 MeV/nucleon, the charge distributions predicted by the model are well fitted by the power-law dependence. For higher energies they begin to resemble exponential dependence. The calculated τ value has a minimum at $E^*/A \approx 4{-}5$ MeV/nucleon. First, consider the solid symbols. The circles represent the inclusive data for $p + \mathrm{Au}$ collisions at 2.16, 3.6, and 8.1 GeV. Here the mean excitation energies are obtained from the fit of the experimental mean IMF multiplicity and the SMM calculations. The diamonds are for $\mathrm{Au} + \mathrm{Au}$ peripheral collisions at 600 MeV/nucleon, excitation energies are estimated by ALADIN collaboration [44] by calorimetric method. The following equation is used in a number of papers to derive the excitation energy from the thermal-like decay products [60]:

$$E = \sum_i^{M_{\mathrm{cp}}} K_i^{\mathrm{cp}} + M_n \langle K_n \rangle + Q + E_\gamma. \tag{1}$$

Here K_i^{cp} are the measured kinetic energies of thermal-like charged particles in the events of multiplicity M_{cp}. To account the unmeasured neutrons, the averaged multiplicity M_n as a model based function of M_{cp} is used, as well as corresponding average neutron kinetic energy $\langle K_n \rangle$. The mass difference of the

final products and the initial state (thermal-like source) is denoted as Q. Energy released in gamma emission (E_γ) is assumed to be rather small. The very important part of the caloric method is the separation between particles emitted during the multi-fragment dissociation and those ejected prior this process. The last ones may be very different in the origin. First of all, these are the cascade particles. They are characterized by the forward peaking angular distribution (in the source frame) and the higher mean energies than thermal-like particles. Cascade particles may be well separated by the properly adjusted energy cutoff. The intranuclear cascade is accompanied by the so-called pre-equilibrium emission caused by particle-hole de-excitation of the residual nucleus just after ejection of cascade particles. The mean energies of pre-equilibrium particles are larger than those for the thermal-like ones, but not so much as for the cascade secondaries. The third source of the ejectiles emitted prior the multibody decay is evaporation from the hot spectator during the thermal expansion (in the spirit of EES model) [12, 41]. We believe that these particles can give the significant admixture to the events selected in caloric method of measuring the excitation energy of the fragment source giving its overestimation. This effect is not considered in Ref. [60], in which the uncertainties involved in the derivation of excitation energy are estimated to be only $\approx 15\%$ for GeV hadron-induced reactions.

The reliability of calorimetric method for heavy ion induced reaction was carefully considered in [63]. It was done for having in mind the properties of the 4π-device INDRA (Caen, France), which is constituted of 336 modules. The event generator SIMON was used to create the events with the well-known properties, which resemble the $\mathrm{Xe} + \mathrm{Sn}$ collisions at 50 MeV/nucleon. These artificial events were filtered by «INDRA filter» to simulate real events. After that the events were reconstructed by calorimetric technique, and obtained properties of the source were compared with the generated ones. It was concluded that it is difficult to have a real experimental mastery of source reconstruction. The excitation energy and excitation energy per nucleon can be measured with accuracy of 10 up to 20%. The estimation of the neutron contribution (unmeasured) remains the main problem. The variance of the excitation energy cannot be measured in fact at all: the «measured» values are several times larger than true ones. This conclusion is especially important for studies of nuclear heat capacity, which is determined [64, 65] via the variance of E according to the relation:

$$C_V = \frac{\sigma_E^2}{T^2} = \frac{\langle E^2 \rangle - \langle E \rangle^2}{T^2}. \tag{2}$$

Let's return to Fig. 10. There is good agreement of the experimental points in Fig. 10 and calculations for excitation energies of up to 7 MeV/nucleon. The deviation for higher energies may be caused by the contribution of the collective flow even in peripheral $\mathrm{Au} + \mathrm{Au}$ collisions. But similar behavior shows the data for the power-law exponent obtained in the study of multifragmentation in the

reaction 8 GeV/c $\pi^- + \mathrm{Au}$ [66]. The data for this case are close to those indicated by diamonds. The thermally induced flow energy for this reaction is estimated in [67]. It is found to be lower than 1 MeV/nucleon for the excitation energies up to 10 MeV/nucleon. Thus, the deviation of the data and model prediction for the fragmentation induced by 8 GeV/c π^- *cannot* be explained by the flow contribution into excitation energy. Therefore, one cannot exclude that estimation of E^*/A by Eq. (1) may be influenced by contribution of the particles emitted before the multifragmentation decay, which are not fully rejected in the procedure of selecting the thermal-like ejectiles. The open points in Fig. 10 are for ^{40}Ar (30 MeV/nucleon) and ^{84}Kr (35 MeV/nucleon) collisions with gold (inclusive data). The measured τ values are lower than the minimal one calculated by SMM. But, as noted in [58], this can be explained by the enhancement of the heavier IMF's caused by another reaction mechanism — dissipative collisions (multinucleon transfer).

Let's return now to Fig. 9. For the central $\mathrm{Au} + \mathrm{Au}$ collisions, the charge distributions (*6* and *7*) are completely different from those discussed just above. They are fitted by the exponential function $Y(Z) \sim \exp(-\alpha Z)$, where the parameter α increases with incident energy. The statistical multifragmentation model does predict the exponential shape of the charge distribution of fragments (instead of the power-law dependence) if the thermal excitation energy exceeds 10 MeV/nucleon. But SMM underestimates the IMF multiplicity: predicted values of α are too large. In the exhaustive paper by Reisdorf et al. [51], the charge distributions for the central $\mathrm{Au} + \mathrm{Au}$ collisions at 150–400 MeV/nucleon are compared with those calculated by SMM, Quantum Statistical Model (QSM) [37], statistical model WIX [38]. None of these models can describe the experimental data: they significantly (several orders of magnitude) underestimate the yield of

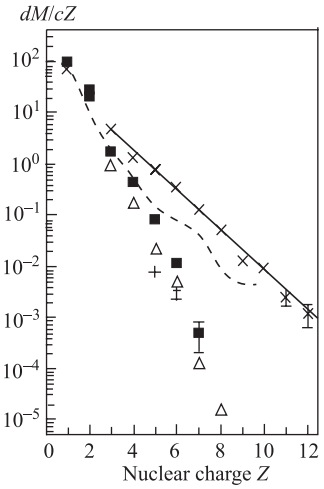

Fig. 11. Comparison of the measured charge distributions (FOPI collaboration, solid line, ×) with calculations using different statistical models: QSM (△), WIX (■), SMM (+). Multifragmentation in the central $\mathrm{Au} + \mathrm{Au}$ collisions at energy 250 MeV/nucleon is considered [51]. The prediction of Isospin Quantum Molecular Dynamic model is indicated by dashed line

heavier IMFs. The implementation of the microscopic Quantum Molecular Dynamic model gives similar results. Figure 11 shows the comparison of the data and model predictions for the beam energy of 250 MeV/nucleon. It is suggested that the higher cluster yield could be explained in the quasi-statistical approach if the density at the moment of fragment formation is around $0.8\rho_0$, i.e., the system is well outside the spinoidal region. As an alternative, this overheated system can be thought of as completely vaporized. According to [51] thermal part of the excitation energy is larger than 20 MeV/nucleon. In that case coalescence (appropriately modified by collective flow) seems to be the proper mechanism of fragment formation from the gaseous phase. In [68], this approach was successfully applied to describe the data for the central $^{20}\mathrm{Ne} + {}^{238}\mathrm{U}$ collisions at 0.25–2.1 GeV/nucleon.

2. THERMAL MULTIFRAGMENTATION

2.1. Time Scale of Thermal Multifragmentation. The time scale of IMF emission is a crucial characteristic for understanding the mechanism of this decay process: whether it is a «slow» successive and independent evaporation of IMF's or a new (multibody) decay mode with almost simultaneous ejection of the fragments governed by the total accessible phase space. «Almost simultaneous» means that all the fragments are liberated during the time which is smaller than the characteristic Coulomb time $\tau_c \approx 10^{-21}$ s (400–500 fm/c) [69], which is the mean time of fragment acceleration in the Coulomb field of the system. In that case, emission of the fragments is not independent. They interact with each other via the Coulomb forces during the acceleration in the common electric field. Thus, measurement of the IMF emission time τ_{em} (the mean time separation between two consecutive fragment emissions) is a direct way to answer the question as to the nature of the multifragmentation phenomenon. In some papers, the mean lifetime of fragmenting system, τ_s, is used to characterize the time scale of the process. There is simple relation between these two quantities [52, 55]:

$$\tau_{\mathrm{em}} = \tau_s/(M-1)\sum_{n=1}^{M-1}\frac{1}{n}. \tag{3}$$

Both the values are close to each other when the mean IMF multiplicity, M, is in the range 2–3, as in the case of the light relativistic projectiles.

There are two procedures to measuring the emission time: analysis of the IMF–IMF correlation function in respect to the relative velocity (see, for example, [70]) or in respect to the relative angle. We used the second method. Figure 12 shows the IMF–IMF relative angle correlation for the fragmentation of target spectator in $^4\mathrm{He}(14.6\ \mathrm{GeV}) + \mathrm{Au}$ collisions [52, 55]. The correlation function exhibits a minimum at $\theta_{\mathrm{rel}} = 0$ arising from the Coulomb repulsion between

the coincident fragments. The magnitude of this effect drastically depends on the time scale of emission, since the longer the time distance between the fragments, the larger their space separation and the weaker the Coulomb repulsion. The multibody Coulomb trajectory calculations fit the data on the assumption that the mean emission time is less than 75 fm/c. This value is significantly smaller than τ_c — the characteristic Coulomb time. Trivial mechanism of IMF emission (independent evaporation) seems to be definitely excluded. Note that Refs. [52, 55] are the first papers with experimental measuring the characteristic time for the thermal multifragmentation, which were followed by a number of similar studies by other groups [71, 72]. Having in mind the importance of the reliable determination of the time-space characteristics of multifragmentation, we consider in some detail our recent studies of this topic for multifragment emission in $p + \mathrm{Au}$ collisions at 8.1 GeV (with FASA setup) [73].

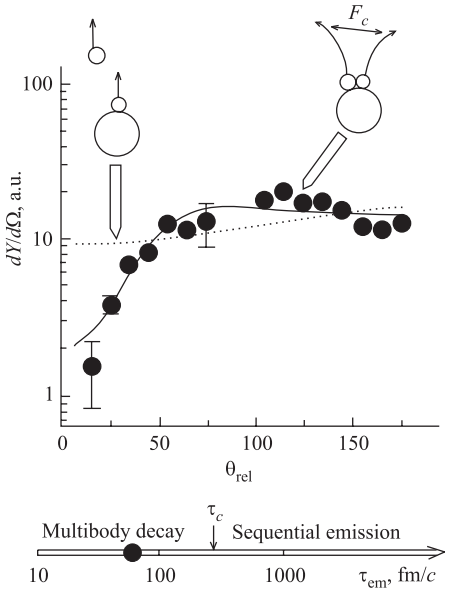

Fig. 12. Measured (symbols) and calculated distributions of relative angles between coincident IMF's for $^4\mathrm{He}(14.6\ \mathrm{GeV}) + \mathrm{Au}$ collisions. Experimental filter of FASA setup corresponds to the detection of $Z_1 > 3$ and $Z > 6$. Solid line is calculated for the simultaneous emission of fragments, dotted line corresponds to the independent evaporation. Time axis (below) is divided into two parts by the Coulomb time τ_c: multibody decay is for $\tau_{\mathrm{em}} < \tau_c$, and sequential evaporation is for $\tau_{\mathrm{em}} > \tau_c$

To study the IMF–IMF correlation as a function of their relative angle, the coincidence yields have been measured for the trigger telescope i and scintillation counter k: $dY_i(\theta_{ik}/d\Omega_k) = Y_{ik}$. The correlation function $C_f(\theta_{\mathrm{rel}})$ is defined as the ratio of Y_{ik} to the counting rate in the same scintillator k, but triggered by the «remote» telescope j, for which $\theta_{jk} > 90°$. Both counting rates are reduced by the number of triggering counts and the contributions of different telescopes i are summed:

$$C_f\left(\theta_{\mathrm{rel}}\right) = C \sum Y\left(\theta_{ik}\right) \frac{N_j}{N_i Y_{jk}}, \tag{4}$$

where $i = 1{-}5$, $k = 1{-}64$ and C is a constant. It is clear that $\theta_{\rm rel} = \theta_{ik}$. The normalization in this formula (by the last term) eliminates the deviations in the efficiency of the counters and compensates the influence of the angular anisotropy with respect to the beam direction. That is similar to the traditional procedure with introducing the counting rate of «mixed» events into the correlation function (see, for example, Refs. [70, 71]).

Theoretical correlation function is obtained with the combined model INC + Exp. + SMM. The Coulomb trajectory calculations are followed for 3000 fm/c. After this amount of time the fragment kinetic energy is close to its asymptotic value. This is demonstrated in Fig. 13 where the mean energies of Be, C, and Mg are shown as a function of $t_{\rm acc}$ — the time interval after the start of the acceleration. The characteristic Coulomb time τ_c is marked, which corresponds to the moment, when fragments reach 90% of their final energy. It is seen from Fig. 13, that the largest part of the IMF kinetic energy is Coulomb in origin. The thermal part is about 10 MeV, it is determined by the mean temperature of the final channel ($\sim 1,5\ T_f$).

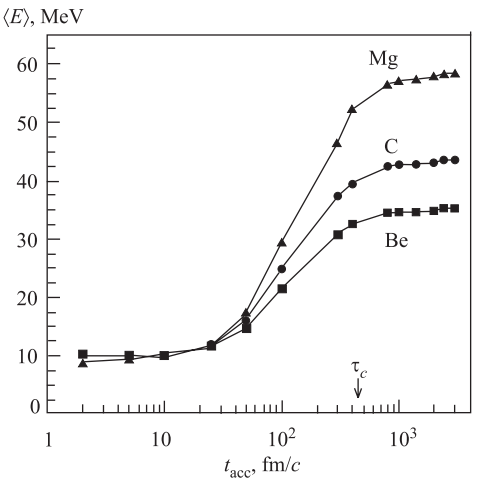

Fig. 13. The calculated mean kinetic energies of Be, C, and Mg as a function of $t_{\rm acc}$, which is the time interval after the start of acceleration

The model dependence of the results was carefully investigated in this paper: *a*) dependence of the results on the mean time of the secondary decay of the hot primary fragments was controlled; *b*) two variants of the combined model have been used for which the properties of the fragmenting nuclei are different; *c*) the sensitivity of the shape of correlation function on the size of the break-up volume was checked.

Let us consider the first point. The primary fragments are hot and their de-excitation is considered by SMM to get the final distributions of cold IMF's. Figure 14 illustrates the significance of this process. It presents the calculated charge distributions of the hot precursors for the final cold fragments with $Z = 4,\ 6,\ 10$. Each distribution has a prominent peak close to these Z values followed by a long tail. One should analyze how the correlation function is sensitive to the assumption about the value of the mean time for the secondary decay. Results are shown in Fig. 15. The experimental correlation function for the intermediate mass fragments (from $p + {\rm Au}$ collisions at 8.1 GeV) is given for events triggered

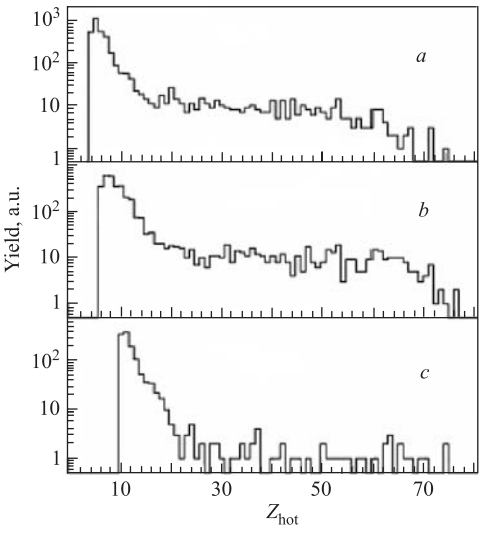

Fig. 14. The calculated distributions of hot primary fragments produced in $p + \mathrm{A}u$ collisions at $E_p = 8.1$ GeV, which are precursors of the cold fragments with $Z = 4$ (*a*), 6 (*b*) and 10 (*c*)

by fragments with $Z \geqslant 6$. This condition was imposed to minimize the influence of the pre-equilibrium emission, which probably takes place for lighter fragments. The calculations (solid and dashed lines) have been performed with INC + Exp. + SMM combined model under two assumptions about τ_{sd} — the mean secondary disintegration time for the fragments: very short, $\tau_{\mathrm{sd}} \ll \tau_c$, and larger than the time of acceleration, $\tau_{\mathrm{sd}} > \tau_c$. In the first case the *cold* fragments are accelerated, as like as it is assumed in MMMC model [36]. In the second variant (solid line) the primary *hot* fragments (with higher charges) propagate through the Coulomb field. One might expect different correlation patterns. The resulting curves deviate not so much from each other. Nevertheless, data are in favor of acceleration of hot fragments.

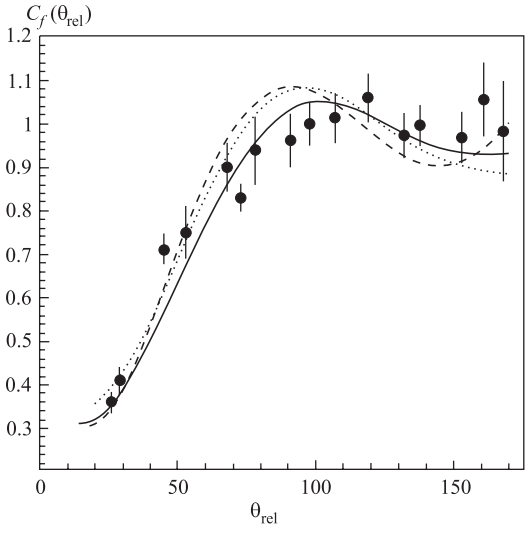

Fig. 15. Relative angle correlation function measured for IMF from p + Au collisions at 8.1 GeV. The lines are model calculated ones for the prompt IMF emission under two assumptions about the mean time of secondary disintegration: $\tau_{\mathrm{sd}} > \tau_c$ (solid line) and $\tau_{\mathrm{sd}} \ll \tau_c$ (dashed line). Dotted line is obtained with another version of the combined model, in which source charge and the excitation energy are 10–15% larger

Dotted line is obtained with slightly changed combined model (see [73]) under assumption $\tau_{\rm sd} > \tau_c$. The comparison of the solid and dotted lines indicates that 10–15% ambiguity in the knowledge of charges and excitation energies of the fragmenting nuclei is not so important (see Table). Note that all the calculations in Fig. 15 are made for prompt fragment emission.

The calculated properties of fragmenting nuclei produced in $p+\mathrm{Au}$ collisions at 8.1 GeV

$\langle M\rangle$	$Z_{M\geqslant 2}$	$A_{M\geqslant 2}$	$E_{M\geqslant 2}$	Model
3.9	72	173	901	INC + SMM
2.16	65	153	616	INC + Exp. + SMM
2.05	70	168	690	INC + Exp.* + SMM

Note. M is the IMF multiplicity, $Z_{M\geqslant 2}$ and $A_{M\geqslant 2}$ are the mean charge and mass numbers of the fragmenting source, $E_{M\geqslant 2}$ is the mean excitation energy (in MeV) corresponding to fragment emission with $M \geqslant 2$

Now let us compare the data with calculations made for different emission times of the system. For each fragment in a given event the starting time to move along a Coulomb trajectory has been randomly chosen according to the decay probability of the system: $P(t) \sim \exp(-t/\tau_{\rm em})$. The calculations were done for $\tau_{\rm em} = 0$, 50, 100, and 200 fm/c. To check the sensitivity of the correlation function to the size of the system, the trajectory calculations have been done for two assumed values of freeze-out volume: $V_f = 8V_0$ and $V_f = 4V_0$. The result is shown in Fig. 16: suppression of the small angles yield becomes only slightly weaker for smaller volume because of some shift of the kinetic energy

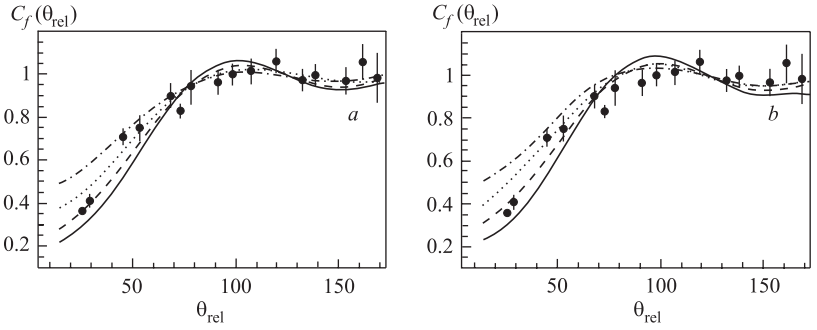

Fig. 16. Comparison of the measured correlation functions (for $p + \mathrm{Au}$ at 8.1 GeV) with the calculated ones for different mean decay times of the fragmenting system. The solid, dashed, dotted, and dash-dotted lines are for $\tau_{\rm em} = 0$, 50, 100, and 200 fm/c. The calculations are made with INC + Exp. + SMM model assuming two values of freeze-out volumes: $8V_0$ (*a*) and $4V_0$ (*b*)

spectrum to higher energies. The mean decay times obtained in these variants of analysis are equal to (50 ± 9) and (37 ± 7) fm/c, respectively. These times are close to the estimated characteristic time of density fluctuations in diluted nucleus, therefore $\tau_{\rm em}$ has been interpreted as characteristic time of the process of fragment formation in diluted system (see, for example, [71]). In the next Section we shall give another understanding of this characteristic of multifragmentation process.

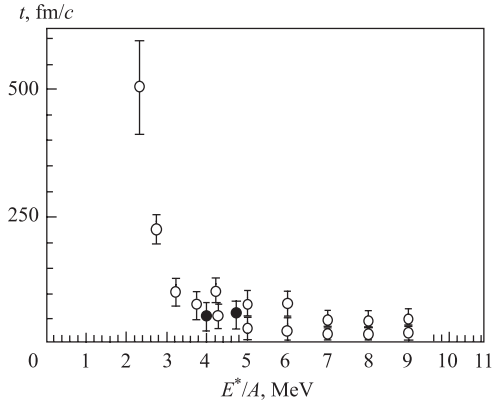

Fig. 17. The measured fragment emission time as a function of the source excitation energy: open circles are for 8 GeV/c $\pi^- + \mathrm{Au}$ [72], filled circles (at 4 and 4.7 MeV) are for p(8.1 GeV) and ^{4}He(14.6 GeV) + Au collisions (FASA data)

The mean decay time of hot nucleus depends on the excitation energy. It has been shown in Ref. [27] that harder collision results in sudden decrease of the decay time caused by the opening of the new reaction channel: multifragmentation replaces the ordinary nucleon evaporation and fission. The same is demonstrated in Fig. 17 for pure thermal multifragmentation. Figure presents the data obtained by IsiS [72] and FASA collaborations [52, 73]. The emission time is shown as a function of the source excitation energy. The last has been measured by the caloric method in Ref. [72]. The excitation energy for FASA data are obtained by the analysis of the IMF multiplicity within the INC + Exp. + SMM model. The transition from the evaporation mode to the multibody decay mode is evident for the excitation energies around 3 MeV per nucleon. The emission time drops down with increase of the excitation energy and achieves a minimum above 3 MeV/nucleon. Similar systematics for heavy ion collisions is given in [74].

2.2. Two Characteristic Volumes in Thermal Multifragmentation. There are a number of papers with estimates of the characteristic volume (or mean density) for multifragmentation process, but the values obtained deviate significantly. A mean freeze-out volume $\sim 7V_0$ (or density of about $\rho_0/7$) was found in Ref. [75] from the average relative velocities of the IMFs at large correlation angles for ^{4}He(14.6 MeV) + Au collisions. The statistical model MMMC [36] was used in this analysis. In paper [80], the nuclear caloric curves were considered within an expanding Fermi gas model to extract average nuclear densities for different fragmenting systems. It was found to be $\sim 0.4\rho_0$ (or $V \approx 2.5V_0$)

for medium and heavy masses. In Ref. [65], the mean kinetic energies of fragments were analyzed by applying energy balance, calorimetric measurements and Coulomb trajectories calculations. The freeze-out volume was found to be $\sim 3V_0$ for the fragmentation in Au $(35\ A \cdot \mathrm{MeV}) + \mathrm{Au}$ collisions. The average source density for the fragmentation in the $8.0\ \mathrm{GeV}/c\ \pi^- + \mathrm{Au}$ interaction was estimated to be $\sim (0.25{-}0.30)\rho_0$ at $E^*/A \sim 5$ MeV from the moving-source-fit Coulomb parameters [76].

In our papers [77, 78], the inclusive and exclusive data on the charge distribution and kinetic energy spectra of IMFs produced in $p(8.1\ \mathrm{GeV}) + \mathrm{Au}$ collisions were analyzed using the statistical model SMM. It was concluded that one should use *two* volume (or density) parameters to describe the multifragmentation process, but not only *one,* as in traditional approach. The first, V_t, corresponds to the stage of fragment formation. Strong interaction between prefragments is still significant at this stage. The second one, V_f, is the freeze-out volume. At this configuration, fragments are well separated from each other, they are interacting via the Coulomb force only. The first parameter is obtained by analyzing the IMF charge distributions, the second one is found via measuring the fragment kinetic energy spectra. Results of these papers are discussed in the next three sections.

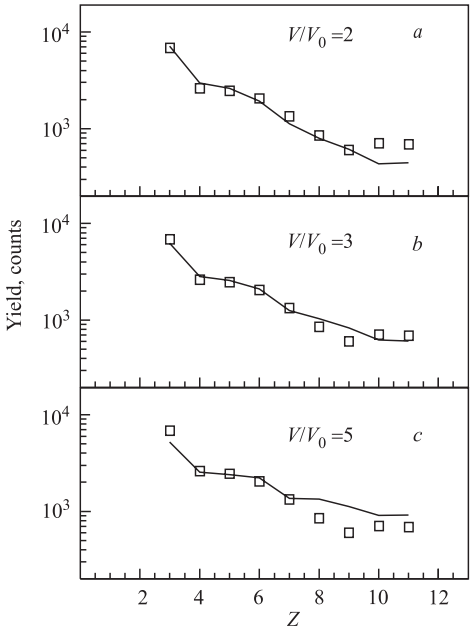

Fig. 18. Charge distributions of intermediate mass fragments measured for $p(8.1\ \mathrm{GeV}) + \mathrm{Au}$ collisions (dots) and calculated with the INC + Exp. + SMM prescription using different values of the system volume, V_t, at the stage of fragment formation

2.2.1. Volume from IMF Charge Distribution. The break-up (or partition) volume is parameterized in the SMM as $V = (1 + k)V_0$. It is assumed in the model that the freeze-out volume, defining the total Coulomb energy of the final channel, coincides in the size with the system volume when the partition is specified. Thus, k is the only volume parameter of the SMM, which also defines (in the first approximation) the free volume ($\approx kV_0$) and the contribution of the translation motion of the fragments to the entropy of the final state. Within this model the probabilities of different decay channels are proportional to their statistical weights (exponentials of entropy).

The entropy is calculated using the liquid-drop model for hot fragments. The statistical model considers the secondary disintegration of the excited fragments to get the final charge distribution of cold IMFs. The importance of the secondary decay stage was considered in Subsec. 2.1.

Figure 18 shows the IMF charge distribution for $p(8.1\ \text{GeV}) + \text{Au}$ collisions measured by a telescope at $\theta = 87°$, provided that at least one more IMF is detected by FMD, the fragment multiplicity detector. Error bars do not exceed the symbol size. The lines are obtained by calculations using the INC + Exp. + SMM prescription under three assumptions about the fragmenting system volume: $2V_0$, $3V_0$, and $5V_0$. Only events with IMF multiplicity $M \geqslant 2$ are considered. The experimental filter of FMD has been taken into account. The theoretical charge distributions are normalized to get the total fragment yield equal to the measured one in the Z range between 3 and 11. A remarkable density dependence of the calculated charge distributions is visible.

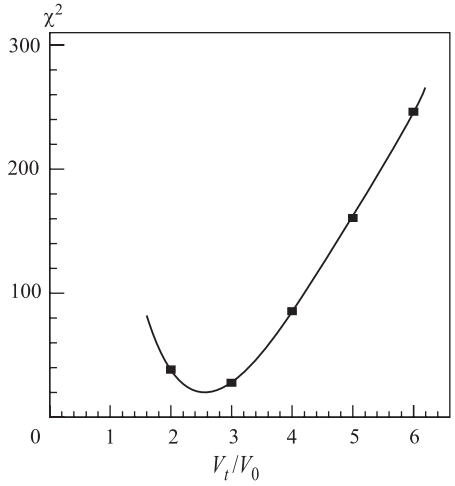

Fig. 19. Value of χ^2 as a function of V_t/V_0 for comparison of the measured and calculated IMF charge distributions. The best fit of the model prediction to the data corresponds to $V_t = (2.6 \pm 0.3)V_0$

The least-square method has been used for quantitative comparison of the data and the calculations. Figure 19 shows the normalized χ^2 as a function of V/V_0. From the minimum position and from the shape of the curve in its vicinity it is concluded that the best fit is obtained with the partition volume $V_t = (2.6 \pm 0.3)V_0$. The error bar (2σ) is statistical in origin. This value corresponds to a mean density of the system $\rho_t = (0.38 \pm 0.04)\rho_0$ (see later why the subscript «t» is used). Analysis of inclusive data gives $V_t = (2.9 \pm 0.2)V_0$.

2.2.2. Size of Emitting Source. Generally, the fragment kinetic energy is determined by thermal motion, Coulomb repulsion, rotation, and collective expansion, $E = E_{\text{th}} + E_c + E_{\text{rot}} + E_{\text{flow}}$. The Coulomb term is about three times larger than the thermal one [73]. The contributions of the rotational and flow energies are negligible for $p + \text{Au}$ collisions [29]. So, the energy spectrum is essentially sensitive to the size of the emitting source. It has been already written above that the kinetic energy spectra are obtained by calculation of multibody Coulomb trajectories, which starts with placing all charged particles of a given decay channel inside the freeze-out volume V_f. Each particle is assigned a thermal

momentum corresponding to the channel temperature. The Coulomb trajectory calculations are performed for 3000 fm/c. After that the fragment kinetic energies are close to the asymptotic values [73]. These calculations are the final step of the INC + Exp. + SMM combined model.

We analyzed carbon spectrum measured by a telescope at $\theta = 87^\circ$ under the condition that at least one additional IMF is detected by FMD. Figure 20 gives a comparison of the measured spectrum with the calculated ones (for emission polar angles $\theta = 87 \pm 7^\circ$). Calculations have been done for the events with $M \geqslant 2$ taking into account the experimental filter of FMD. The energy ranges of the spectra are restricted to 80 MeV to exclude the possible contribution of pre-equilibrium emission. The calculations are performed with a fixed partition volume, $V_t = 2.6\ V_0$, in accordance with the findings of the previous section. The freeze-out volume, V_f, is taken as a free parameter. Figure 20 shows the calculated spectra for V_f/V_0 equal to 3, 6, and 13. The least-square method is used to find the value of V_f corresponding to the best description of the data.

Figure 21 presents χ^2 as a function of V_f/V_0. From the position of its minimum one gets $V_f = (5.0 \pm 0.5)V_0$ (or mean freeze-out density $\rho_f \approx 0.2\rho_0$).

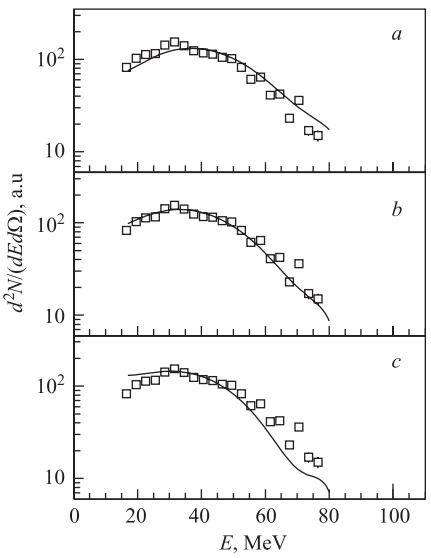

Fig. 20. Kinetic energy spectrum of carbon (at $\theta = 87^\circ$) emitted by the target spectator in $p(8.1\ \text{GeV}) + \text{Au}$ collisions. Lines are calculated under assumption of $V_t = 2.6\,V_0$. The freeze-out volume, V_f, is taken to be equal to 3 (*a*), 6 (*b*), and $13\,V_0$ (*c*)

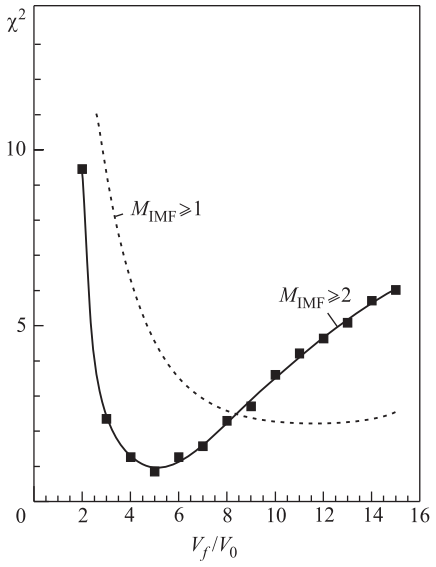

Fig. 21. Value of χ^2 as a function of the freeze-out volume V_f/V_0 for comparison of the measured and calculated kinetic energy spectra of carbon. The solid line is for the events with IMF multiplicity $M \geqslant 2$. The best fit corresponds to $V_f = (5.0 \pm 0.5)V_0$

Systematics provides the main contribution to the error of this estimation of the freeze-out volume. It is caused by a 3% uncertainty in the energy scale calibration.

In paper [77], the value $V_f = (11 \pm 3)V_0$ was obtained by analyzing the inclusive energy spectrum of carbon. This great difference may be explained by the fact that SMM overestimates fragment energies for the events with $M = 1$ [79]. As a result, the fitting procedure shifts V_f to the larger values. This observation of Ref. [79] is illustrated by Fig. 22, which presents the main characteristics of the kinetic energy spectrum of carbon produced in $p + \mathrm{Au}$ collisions at 8.1 GeV.

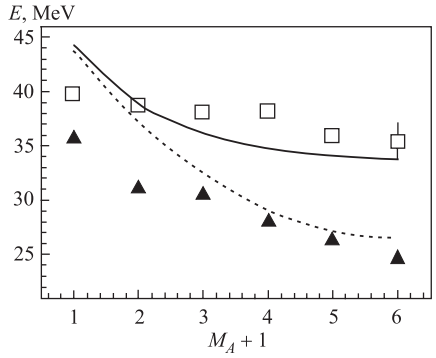

Fig. 22. Mean energy (□) and $E_{\max}$ (▲) of carbon isotopes as a function of IMF multiplicity for $p(8.1\ \mathrm{GeV}) + \mathrm{Au}$ collisions. Symbols are the experimental data, the lines are calculated with INC + Exp. + SMM and folded with the experimental filter: solid line — $\langle E \rangle$; dashed line — $E_{\max}$

The mean energy and maximum position are shown as a function of the IMF multiplicity M_A detected by fragment multiplicity detector of the FASA setup. The mean energy is slightly decreasing with M_A in contrast to the model calculation. Especially remarkable deviation is observed for M_A equal to 0 and 1: model predicted mean energy change is about 10 MeV, experimentally observed one is almost ten times less. The probable explanation of this observation may be the following. The model predicts the existence of heavy residual for the events with fragment multiplicity $M = 1$ ($M_A = 0$). An only fragment created in the event should be treated as evaporated from the surface of this residual. In fact, this scenario is not realized, heavy residual is destroyed somehow (by secondary fission, for example) and Coulomb field for detected carbon is reduced.

2.2.3. Multifragmentation and Nuclear Fission (Scission). The existence of two different size characteristics for multifragmentation has a transparent meaning. The first volume, V_t, corresponds to the partition point (or fragment formation stage), when the properly extended hot target spectator transforms into a configuration consisting of specified prefragments. They are not yet fully developed, there are still links (nuclear interaction) between them. The final channel of disintegration is completed during the evolution of the system up to the moment when receding and interacting prefragments become completely separated. This is just as in ordinary fission. The saddle point (which has a rather compact shape)

resembles the final channel of fission by way of having a fairly well-defined mass asymmetry. Nuclear interaction between fission prefragments ceases after descent of the system from the top of the barrier to the scission point. In papers by Lopez and Randrup [81] the similarity of both processes was used to develop a theory of multifragmentation based on suitable generalization of the transition-state approximation first considered by Bohr and Wheeler for ordinary fission in 1939. The theory is able to calculate the potential energy as a function of the r.m.s. extension of the system, yielding the space and energy characteristics of the transition configuration, and the barrier height for fragmentation. The transition states are located at the top of the barrier or close to it. The phase space properties of the transition states are decisive for the further fate of the system, for specifying the final channel.

Being conceptually similar to the approach of Ref. [81], the statistical model of multifragmentation (SMM) uses the size parameter, which can be determined by fitting to data. The size parameter obtained from the IMF charge distribution can hardly be called a freeze-out volume. In the spirit of the papers by Lopez and Randrup we suggest the term «transition state volume», $V_t = (2.6 \pm 0.3)V_0$. The larger value of the size parameter obtained by the analysis of the kinetic energy spectra is a consequence of the main contribution of Coulomb repulsion to the IMF energy, which starts to work, when the system has passed the «multiscission point» (see Fig. 23). Thus, $V_f = (5.0 \pm 0.5)V_0$ is the freeze-out volume for multifragmentation in $p + \mathrm{Au}$ collisions. It means that the nuclear interaction between fragments is still significant when the system volume is equal to V_t, and only when the system has expanded up to V_f, are the fragments freezing out. In the statistical model used, the yield of a given final channel is proportional to the corresponding statistical weight. Therefore, the nuclear interaction between prefragments is neglected when the system volume is V_t, and this approach can be viewed as a rather simplified transition-state approximation. Nevertheless, the SMM describes well the IMF charge (mass) distributions for thermally driven multifragmentation. Note once again, that in the traditional application of the SMM only one size parameter is used, which is called «freeze-out volume». The shortcoming of such a simplification of the model is obvious now.

The values of V_t and V_f may be sensitive to the way of their estimation. One could imagine that the freeze-out volume V_f might be estimated by a model independent method, if the experimental data on the source Z value and charge distribution in the final channel were known. After that one needs to calculate the multibody Coulomb trajectory (with V_f as a single free parameter) to get fragment energies. But it is true only for the case when the fragments are already cold after scission point as in MMMC model [36]. Moreover, the heaviest undetected fragments should be included in trajectory calculations. It can be done either on the model basis or by some arbitrary assumption. As for V_t, we do not see any possibility of finding it in a model-independent way. We know that it is a key

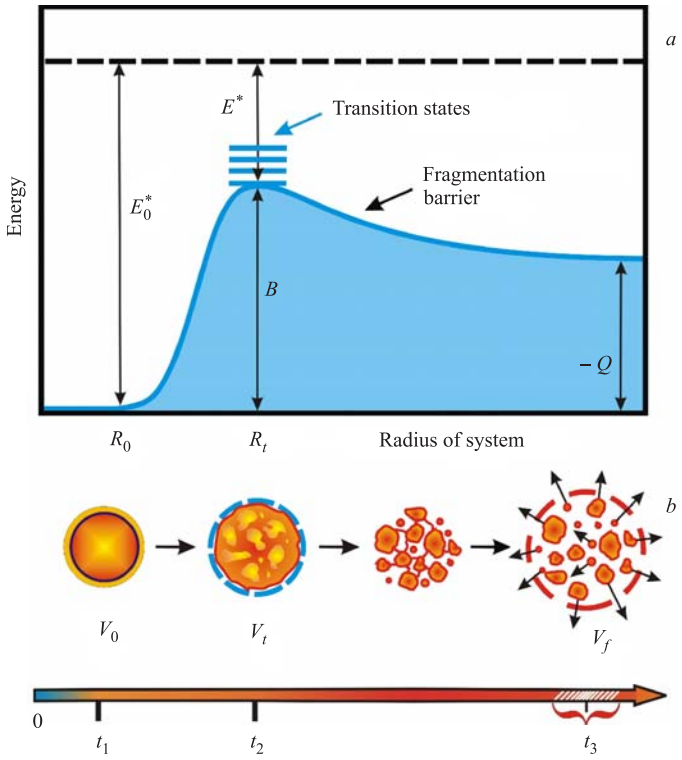

Fig. 23. *a*) Qualitative presentation of the potential energy of the hot nucleus (with excitation energy E_0^*) as a function of the system radius. Ground state energy of the system corresponds to $E = 0$, B is the fragmentation barrier, Q is the released energy. *b*) Schematic view of the multifragmentation process and its time scale

parameter for defining the fragment charge distribution, and one should look for other observables that are also sensitive to the V_t value.

In a recent paper by Campi et al. [82], the «little big bang» scenario of multifragmentation is suggested in which fragments are produced at an early, high temperature and high density stage of the reaction (see also [83–85]). This scenario is very impressive, but it is not yet a well-finished model that could be compared directly with experimental data.

The evidence for the existence of two characteristic volumes of multifragmentation changes understanding the time scale of the process (see Fig. 23, *b*). Now one can imagine the following ingredients of the time scale: t_1 — the mean thermalizataion time of the excited target spectator, t_2 — the mean time

of the expansion to reach the transition state, $(t_3 - t_2)$ — the mean time of descent of the system from the top of the barrier to the multiscission point. The system configuration on the way to the scission point is composed of several prefragments connected by necks. Their random rupture is characterized by the mean time, τ_n, which is an important ingredient of fragment emission time, $\tau_{\rm em}$. Another ingredient of $\tau_{\rm em}$ is characteristic time of the density fluctuations in the transition state, τ_t. So, $\tau_{\rm em} \approx (\tau_t^2 + \tau_n^2)^{1/2}$. Formally, $\tau_{\rm em}$ may be understood as the standard deviation of t_3: $\tau_{\rm em} = (\langle t_3^2 \rangle - \langle t_3 \rangle^2)^{1/2}$. In the earlier papers, the emission time was related only to time characteristic of density fluctuations in the system at the stage of fragment formation, i.e., at $t \approx t_2$. The actual picture is much more complex.

What are the expected values of these characteristic times? Thermalization or energy relaxation time after intranuclear cascade, t_1, is model estimated to be 10–20 fm/c [86, 87]. Expanding Emitting Source model (EES) predicts $\langle t_2 - t_1 \rangle \approx 70$ fm/c for $p(8.1$ GeV$) + $Au collisions [12]. In this model, it is assumed that $t_2 \approx t_3$. Fragment emission time, $\tau_{\rm em}$, is measured in many papers to be ≈ 50 fm/c. The density fluctuation time, τ_t, is model estimated to be 30–40 fm/c [88–90]. Calculation within the BNV model results in estimation of t_3 to be equal to 150–200 fm/c [91]. A new theoretical consideration of the partition dynamics of very hot nuclei is needed. It is especially important to find a way to measure the value of t_3.

Note, that in the case of ordinary fission t_2 is specified by the fission width Γ_f, which corresponds to the mean time of order of 10^{-19} s (or $\sim 3.3 \cdot 10^4$ fm/c) for the excitation energy around 100 MeV [92]. The value t_3 was model estimated in a number of papers (e.g., [94]): $t_3 \approx 1000$ fm/c. A mean neck rupture time is estimated in [95] within the model of Rayleigh instability:

$$\tau_n = [1.5(R_n/\text{fm})^3]^{1/2} \cdot 10^{-22} \text{ s}. \tag{5}$$

Generally, the values of τ_n are found to be less than 300 fm/c. Using Eq. (5) for the estimation of the mean time for the rupture of multineck configuration in fragmentation, one gets τ_n between 40 and 115 fm/c under assumption of the neck radius R_n between 1 and 2 fm. These estimations are in qualitative agreement with the measured values of the fragment emission time $\tau_{\rm em}$.

As for the space characteristics, the relative elongation of the very heavy systems ($Z > 99$) at the fission scission point is similar to that for the multiscission point of medium hot nuclei (rare-earth region). For the fission of the lighter nuclei, (Po–Ac), the scission elongation is larger [95].

2.3. Comparative Study of Fragmentation Induced by Relativistic Protons, ^{4}He, and ^{12}C. It has been already told in Sec. 1, that the multifragment emission in the central collisions of very heavy ions is not described by the statistical models. Initial compression of the system is tremendous and the collective part

of the excitation energy is so large that the partition of the system into fragments is likely to be a very fast dynamic process [51]. In that case the fragment kinetic energy is largely determined by the collective flow. It is interesting to follow the evolution of the multifragmentation mechanism (as the projectile mass increases) from pure thermal to that influenced by the dynamic effects. The comparative study of multifragmentation induced in a gold target by different relativistic projectiles (protons, helium and carbon ions) has been performed in Refs. [28, 29], which will be followed below. First of all, it is demonstrated that in all the cases one deals with disintegration of a thermally equilibrated systems. In the same time, the fragment kinetic energy spectra are changing with increasing of the projectile mass. The spectral shapes show an increase in the number of high-energy fragments for heavier projectiles. This observation is summarized in Fig. 24, *a*, which shows the mean kinetic energies per nucleon as a function of the fragment charge. The figure reveals remarkable enhancement in the kinetic energies for the light fragments ($Z < 10$) emitted in $^{4}\mathrm{He}(14.6\ \mathrm{GeV}) + \mathrm{Au}$ and $^{12}\mathrm{C}(22.4\ \mathrm{GeV}) + \mathrm{Au}$ collisions as compared to the $p(8.1\ \mathrm{GeV}) + \mathrm{Au}$ case. The calculated values (lines) are obtained with the INC+Exp.+SMM combined model. The measured energies are close to the calculated ones for $p+\mathrm{Au}$ collisions in the range of fragment charges between 4 and 9. However, the experimental values for heavier projectiles exceed the theoretical ones, which are similar for all three cases. What is the cause for that?

Note once again that the kinetic energies of fragments are determined by four terms: thermal motion, Coulomb repulsion, collective rotation, and expansion energies, $E = E_{\mathrm{th}} + E_C + E_{\mathrm{rot}} + E_{\mathrm{flow}}$. The contribution of the rotational energy is estimated to be negligible even for $^{12}\mathrm{C} + \mathrm{Au}$ collisions. It is suggested that the observed energy enhancement is caused by the radial expansion flow in the system. Note, that the contribution of the collective flow for $p(8.1\ \mathrm{GeV}) + \mathrm{Au}$ collisions is inconspicuous [12]. It is believed, that the observed flow for heavier projectiles is driven by the thermal pressure, which is larger than for the proton beam because of higher initial temperature.

An estimate of the fragment flow energies may be obtained as a difference between the measured IMF energies and the model calculated ones without any flow in the system. This difference for ^{12}C + Au collisions is shown in Fig. 24, *b*. Data in Fig. 24 are obtained for polar angle $\theta = 87^{\circ}$. The similar results are obtained for $\theta = 24^{\circ}$ and 156° indicating that the flow is radial one.

In an attempt to describe the data we modified the SMM code in the $\mathrm{INC} + \mathrm{Exp.} + \mathrm{SMM}$ concept by including a radial velocity boost for each particle at freeze out. In other words, the radial expansion velocity was superimposed on the thermal motion in the calculation of the multibody Coulomb trajectories. Self-similar radial expansion is assumed, when the local flow velocity is linearly dependent on the distance of the particle from the center of mass. The expansion velocity of particle Z located at radius R_Z is given by the following expression:

$$v_{\rm flow}(Z) = v^0_{\rm flow} R_Z / R_{\rm syst}, \tag{6}$$

where $v^0_{\rm flow}$ is the radial velocity on the surface of the system. Note that in this case the density distribution is changing in dynamic evolution in a self-similar way being a function of the scaled radius $R_Z/R_{\rm syst}$. The use of the linear profile of the radial velocity is motivated by the hydrodynamic model calculations for

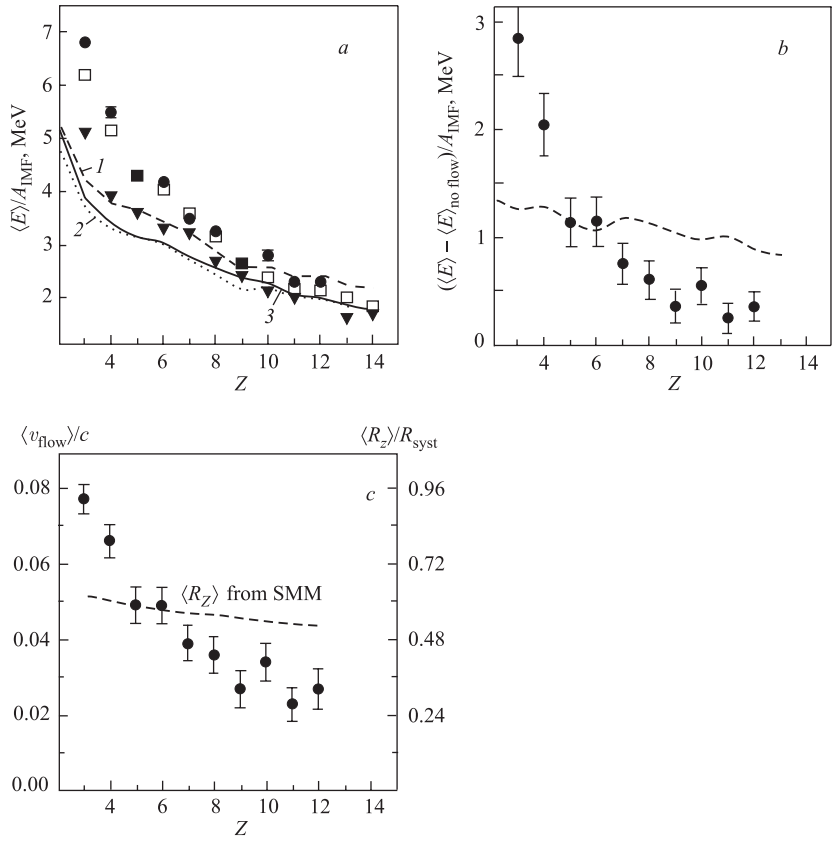

Fig. 24. *a*) Mean kinetic energies of fragments per nucleon measured at $\theta = 87^\circ$ for $p(8.1$ GeV) (▼, *1*), ^{4}He(14.6 GeV) (□, *2*), and ^{12}C(22.4 GeV) (●, *3*) collisions with Au. The lines are calculated within INC + Exp. + SMM approach assuming no flow. *b*) Flow energy per nucleon (dots) obtained as a difference of the measured fragment kinetic energies and the values calculated under assumption of no flow in the system. The dashed line represents a calculation assuming a linear radial profile for the expansion velocity with $v^0_{\rm flow} = 0.1c$. *c*) Experimentally deduced mean flow velocities (dots) for ^{12}C + Au collisions as a function of the fragment charge, and the mean relative radial coordinates of fragments (right scale). The dashed line shows the mean radial coordinate according to SMM

an expanding hot nuclear system. The value of $v^0_{\rm flow}$ was adjusted to describe the mean kinetic energy measured for the carbon fragments.

Figure 25 shows the comparison of the measured and calculated energy spectra of carbon fragments from $^{12}\mathrm{C}(22.4\ \mathrm{GeV}) + \mathrm{Au}$ collisions assuming $v^0_{\rm flow} = 0.1c$. The agreement is very good. The calculation without a flow deviates strongly.

There is a longstanding problem of a qualitative difference between the chemical or thermal equilibrium temperature and the «kinetic» or the so-called «slope temperature». An alternative explanation of this observation is given in Ref. [93] in which the slope temperature is related to the nuclear Fermi motion. Figure 25 presents less exotic interpretation of this puzzle. The mean equilibrium temperature obtained in our calculations is $\sim$ 6 MeV. At the same time, the slope temperature found from the calculated spectrum shape is $T_s = 14.5$ MeV for the «no flow» case (see dashed curve in insert). This is the mutual result of the thermal motion, Coulomb repulsion during the volume disintegration, and the secondary decay of the excited fragments. Introducing a rather modest radial flow results in an increase of the slope temperature up to $T_s = 24$ MeV in accordance with the data.

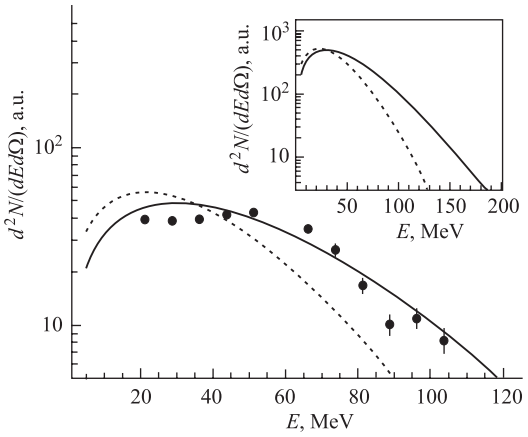

Fig. 25. Energy distribution of carbon fragments (at $\theta = 87^\circ$) from $^{12}\mathrm{C} + \mathrm{Au}$ collisions. Solid lines are calculated assuming the radial flow with the velocity on the surface equal to $0.1c$. Dashed lines are calculated assuming no flow

Let's return to Fig. 24, *b*. The model-calculated flow energy is given as a difference of the calculated fragment energies obtained for $v^0_{\rm flow} = 0.1c$ and $v^0_{\rm flow} = 0$. The data deviate significantly from the calculated values for Li and Be. It may be caused in part by the contribution of particle emission during the early stage of expansion from a hotter and denser system (pre-equilibrium emission). This explanation is supported by the fact that the extra energy of Li fragments with respect to the calculated value is clearly seen in Fig. 24, *a* even for the proton-induced fragmentation, where no significant flow is expected. As to fragments heavier than carbon, the calculated curve in Fig. 24, *b* is above the data and only slightly goes down with increasing fragment charge. This trend of the calculations is to be expected. The mean fragment flow energy is proportional to $\langle R_Z \rangle$. This value varies only slightly with the fragment charge in the SMM code due to the

assumed equal probability for fragments of a given charge to be formed at any point of the available break-up volume. This assumption is a consequence of the model simplification that considers the system as a uniform one with $\rho(r) = \text{const}$ for $r \leqslant R_{\text{syst}}$. The data indicate that it is not the case. In fact, the dense interior of the expanded nucleus may favor the appearance of larger IMF's, if fragments are formed via the density fluctuations. This observation is also in accordance with the analysis of the mean IMF energies performed in [12] for proton induced fragmentation. It is also seen in Fig. 24, *a* that for $p + \text{Au}$ collisions the measured energies are below the theoretical curve for fragments heavier than Ne. This may be explained by the preferential location of the heavier fragments in the interior region of the freeze-out volume, where the Coulomb field is reduced.

The experimentally deduced mean flow velocities of IMF's for $^{12}\text{C} + \text{Au}$ collisions are presented in Fig. 24, *c*. The values for Li and Be are considered as upper limits because of the possible contribution of the pre-equilibrium emission. The corresponding values of $\langle R_Z/R_{\text{syst}}\rangle$, obtained under the assumption of the linear radial profile for the expansion velocity, can be read on the right-hand scale of Fig. 24, *b*. The dashed line shows the mean radial coordinates of the fragments according to the SMM code. The calculated values of $\langle R_Z/R_{\text{syst}}\rangle$ are only slightly decreasing with Z in contrast to the data.

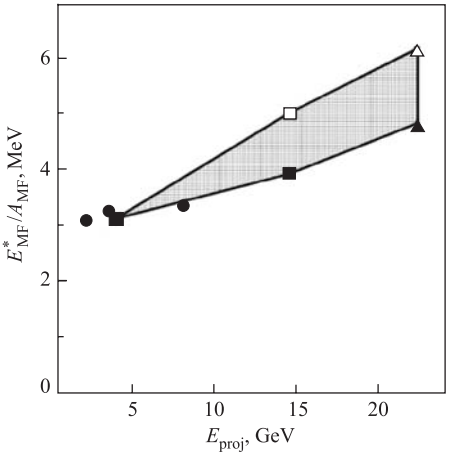

Fig. 26. Mean excitation energy of the fragmenting nucleus $E^*_{\text{MF}}/A_{\text{MF}}$ as a function of the beam (proton (●), helium (■), and carbon (▲)) energy: the solid points refer to the thermal part, the flow energy added is shown as open symbols and grey area

The total expansion energy can be estimated by integrating the nucleon flow energy over the available volume at freeze out. For uniform system one gets:

$$E^{\text{tot}}_{\text{flow}} = (3/10)A\, m_N (v^0_{\text{flow}})^2 (1 - r_0/R_{\text{syst}})^5, \tag{7}$$

where m_N and r_0 are the nucleon mass and radius. For $^{12}\text{C} + \text{Au}$ collisions it gives $E^{\text{tot}}_{\text{flow}} \cong 115$ MeV, corresponding to the flow velocity on the surface equal to $0.1c$.

Similar results are obtained for $^4\text{He}(14.6\text{ GeV}) + \text{Au}$ collisions. The excitation energies of the fragmenting systems studied are largely thermal ones, therefore we deal with the thermal multifragmentation. It is reflected in Fig. 26, where the mean total excitation energies per nucleon, $E_{\text{MF}}/A_{\text{MF}}$, are shown as

a function of the incident energy. The full symbols correspond to the thermal part of the excitation energy obtained via analysis of the data on fragment multiplicity and charge distributions with the combined model of the process. Open symbols include the flow energy. Thermal energies for these cases are four times larger than collective ones. The onset of the collective flow driven by the thermal pressure takes place at the excitation energy around 4 MeV/nucleon, which is in good agreement with the results of [67]. The estimated mean fragmenting masses are equal to 158, 103, 86 for proton (8.1 GeV), ^{4}He (14.6 GeV), and ^{12}C (22.4 GeV) collisions with Au, respectively. Note that the data given in Fig. 26 are inclusive, selection of the events with the IMF multiplicity $M \geqslant 2$ (as in the correlation measurements) results in an increase of the mean excitation energy by 0.5–0.7 MeV/nucleon [73].

The charge distributions of fragments have been found to be similar for all the collisions studied, and they are very well described by the combined INC + Exp. + SMM model (Fig. 27). The general trend of the IMF charge distributions is also well reproduced by power law $Y(Z) \sim Z^{-\tau}$. In the earlier papers on multifragmentation [6, 8, 96, 97] such dependence for the fragment charge yield was interpreted as an indication of the proximity to the critical point for the liquid–gas phase transition in nuclear matter. This was stimulated by the application of the classical Fisher drop model [98], which predicted a pure power law droplet-size distribution with the minimal value of $\tau = 2{-}3$ at the critical point for the liquid–gas phase transition. So, in the spirit of the Fisher model, the data in the insert of Fig. 27 should be considered as an indication of the

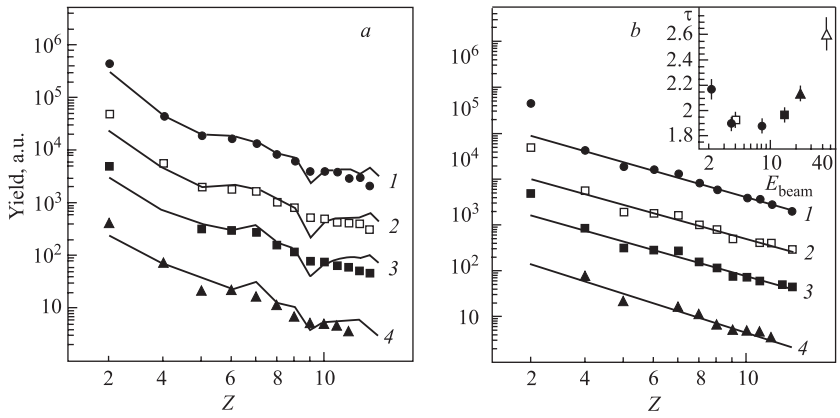

Fig. 27. Fragment charge distributions obtained at $\theta = 87^\circ$ for p + Au at 8.1 GeV (*1*), ^{4}He + Au at 4 GeV (*2*), ^{4}He + Au at 14.6 GeV (*3*) and ^{12}C + Au at 22.4 GeV (*4*). The lines (*a*) are calculated by INC + Exp. + SMM (normalized at $Z = 3$). The power law fits are shown on the right panel with τ parameters given in the insert as function of the beam energy. The last point in the insert is for ^{12}C + Au collisions at 44 GeV (FASA data)

«critical behavior» of the system. But, it is not the case. The power law is well explained at temperatures far below the critical point [99]. As is seen in Fig. 27, the pure thermodynamic model predicts that the IMF charge distribution is close to a power law at the system temperature of 5–6 MeV, while the critical one is assumed to be $T_c = 18$ MeV. The more realistic consideration of the problem of phase transitions in hot nuclei is given in the next Section.

Concluding Subsec. 2.3, the study of multifragmentation using a range of relativistic projectiles demonstrates a transition from pure «thermal decay» (for $p + \mathrm{Au}$ collisions) to disintegration «decorated» by the onset of a collective flow (for heavier projectiles). Nevertheless, the decay mechanism should be considered as thermal multifragmentation. The partition of the system is governed by the nuclear heating, and IMF charge distributions in all the cases considered are well described by the statistical model neglecting any flow. The modest flow energy (of an order of MeV/nucleon) does not change the mechanism of hot nucleus disintegration. The flow energy of fragments decreases as their charge increases. The analysis of the data reveals interesting information on the fragment space distribution inside the break-up volume: heavier fragments are formed predominantly in the interior of the fragmenting nucleus possibly due to the density gradient. This conclusion is in contrast to the predictions of the statistical multifragmentation model.

Similar comparative study of target multifragmentation was performed by MULTI collaboration using relativistic protons, ^{16}O, ^{20}Ne, and ^{28}Si [100]. The array consisting of a number of the Bragg chambers has been used. The remarkable evolution of the IMF spectrum shapes is also observed and studied in detail: Coulomb peaks become wider and high-energy tails become longer as projectile mass increases. The angular distributions in all the cases show the existence of sideward-peaking component for fragments with $Z \geqslant 10$. It should be noted, that the first experimental indication of this effect was obtained 30 years ago with relativistic proton beams [101–103]. Several interpretations of sideway peaking have been proposed, the most intriguing one is the nuclear shock wave. But it seems to be more realistic to explain the sideward peaking by the kinematics effect related to the significant transverse velocity of heavy residue of the intranuclear cascade. It was demonstrated by INC calculations in Ref. [104]. This effect was carefully investigated later in Ref. [105] for multifragmentation induced in gold target by 10–14.6 GeV protons. A two-step cascade and statistical multifragmentation calculation is consistent with the data without invoking any exotic ideas.

3. MULTIFRAGMENTATION AND PHASE TRANSITIONS IN HOT NUCLEI

3.1. Nuclear Liquid, Nuclear Fog, Nuclear Gas, and Critical Temperature. One of the first nuclear models was the liquid-drop model (LDM), suggested by

N. Bohr, K. Weizsaecker, and Ya. I. Frenkel $\sim$ 70 years ago. It is successfully used up to now. The modern atomic mass formulas, based on the LDM, describe the nuclear masses with accuracy better than 10^{-5}. This model was invented to understand the nuclear fission phenomenon, and nowadays LDM is the firm basis for the creation of the new refined fission theories. About 30 years ago, it has been understood that there is a great similarity of the equation of the state for the classical and nuclear systems. The physical reason for that is the similarity between the Van der Waals and nucleon–nucleon interactions. In both cases the attraction between particles is replaced by repulsion at a small interaction range. Notwithstanding the tremendous difference in the energy and space scales, the equations of state are as like as two peas in a pod. It is well seen in the phase diagram (Fig. 28), prepared using Ref. [106]. J. D. Van der Waals suggested his famous equation in 1875. Hundred years later his finding was used fruitfully to describe properties of the nuclear media unknown for scientists of the nineteenth century.

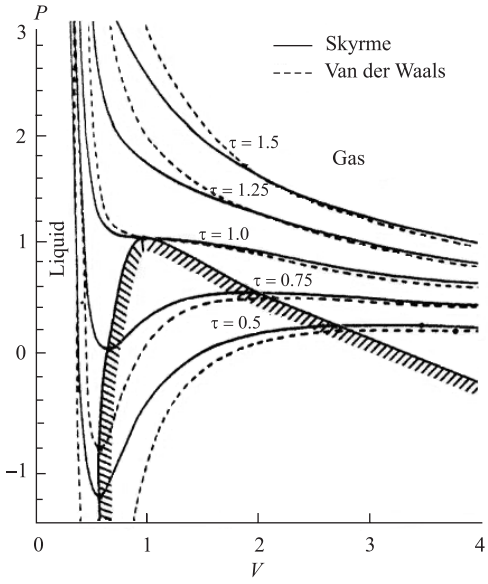

Fig. 28. Comparison of the equation of state for the Van der Waals gas and for a nuclear system interacting through a Skyrme force (the relative units are used). Spinodal region is below the hatched line

Figure 28 shows the isotherms for pressure as a function of volume calculated for the Van der Waals system and for the system of nucleons interacting through Skyrme force. The scales are the same for both cases due to the use of dimensionless variables: pressure, volume and temperature are given as ratios to the critical values P_c, $V_c = 1/\rho_c$, and T_c. The very steep part of the isotherms (on the left side) corresponds to the liquid phase. The gas phase is presented by the right parts of the isotherms where pressure is changing smoothly with increasing volume. The critical isotherm is marked by $T = 1$, it has specific inflection point. The surface tension vanishes at T_c, and only gas phase is possible above this temperature. Of the peculiar interest for the topic of this review is the part of the diagram, which is below the hatched line, where the isotherms correspond to the negative compressibility, $\partial P/\partial V\big|_T > 0$. The density here is significantly reduced as compared to the liquid phase. This is a spinodal region characterized by the phase

instability. The top of the spinodal region is the critical point for the liquid–gas phase transition (critical temperature $\times$ critical volume). One can imagine that a hot nucleus expands due to thermal pressure and enters into the metastable region. Due to density fluctuations, a homogeneous system converts into the mixed-phase state, consisting of droplets (IMF's) surrounded by nuclear gas (nucleons and light composite particles). In fact, the final state of this transition is a *nuclear fog*.

This term was introduced by Siemens in 1984 [6, 108], when the main problems of the field were only discussed. Figure 29 is taken from Ref. [108] to illustrate three possible scenarios of disintegration of hot (and compressed) nucleus in dependence on the temperature of the system. For the low temperatures, panel *a*, one should expect the monopole vibration of nucleus accompanied by particle evaporation. The amplitude of this vibration is modest one, the pressure is changing the sign periodically. The picture becomes completely different with increase of the temperature, when system crosses the line of hydrodynamic instability, at which $\partial P/\partial V\big|_S = 0$, scenario *b*. Beyond this line, inside the spinodal region, the small density fluctuations grow very fast, and there is no barrier to prevent the system from separating into two phases. Nucleons associate themselves with nascent droplets or bubbles leading to the formation of *nuclear fog*, which explodes because of the Coulomb repulsion to be detected as multifragmentation.

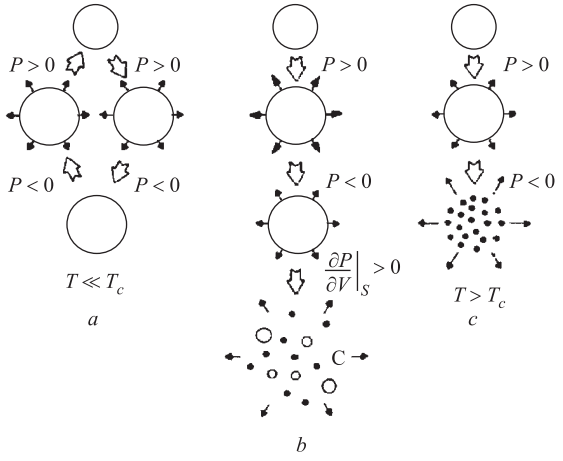

Fig. 29. Scenarios of nuclear expansion: *a*) monopole vibration at low excitation; *b*) explosion to liquid–gas phase mixture (nuclear fog) at $T < T_c$; *c*) explosion to gas at $T \geqslant T_c$

Figure 29, *c* describes the fate of very hot nucleus with the temperature higher than critical one for the liquid–gas phase transition, $T > T_c$. The internal pressure of the liquid causes it to expand nearly isentropically. The pressure accelerates

the matter outwards being all the time positive. The internal energy is converted (in part) into the radial collective flow energy. The matter cools as it expands, but it remains hotter than T_c, until its density is much smaller than ρ_0. Finally, it becomes a free streaming, non interacting gas. That is a pure case of the *liquid–gas* phase transition. The intermediate mass fragments can be observed even for so high temperature of the system, but because of the secondary effect of coalescence from the gas phase (see, e.g., [68]). Thus, the critical temperature is a key parameter to specify the mechanism of IMF production.

There are many calculations of T_c for finite nuclei. In [109–111], for example, it is done by using a Skyrme effective interaction and the thermal Hartree–Fock theory. The values of T_c were found to be in the range 10–20 MeV depending upon the chosen Skyrme interaction parameters and the details of the model.

The main source of the experimental information for T_c is the fragment yield. In some statistical models of nuclear multifragmentation the shape of the IMF charge distribution, $Y(Z)$, is sensitive to the ratio T/T_c. It has been already noted, that the fragment charge distribution is well described by the power law $Y(Z) \sim Z^{-\tau}$, as predicted by the classical Fisher droplet model [98] for vicinity of the critical point. In Ref. [8], Hirsch et al. estimate T_c to be ~ 5 MeV simply from the fact that the IMF mass distribution is well described by a power law for the collision of p (80–350 GeV) with Kr and Xe. In paper by Panagiotou et al. [96] the experimental data were gathered for different colliding systems to get the temperature dependence of the power-law exponent. As a temperature, the inverse slope of the fragment energy spectra was taken in the range of the high-energy tail. The minimal value of τ was obtained at $T = 11{-}12$ MeV, which was claimed as T_c. The later data smeared out this minimum. Moreover, it became clear that the «slope» temperature for fragments does not coincide with the thermodynamic one, which is significantly smaller (see discussion in Subsec. 2.3).

A more sophisticated use of Fisher's model for the estimation of T_c has been made in [112]. The model is modified by including the Coulomb energy release, when a particle moves from the liquid to the vapor. The data for multifragmentation in π $(8$ GeV$/c) + \mathrm{Au}$ collisions were analyzed. The extracted critical temperature was (6.7 ± 0.2) MeV. The same analysis technique was applied to the data for the multifragmentation in collisions of Au, La, Kr (at 1.0 GeV/nucleon) with a carbon target [113]. The extracted values of T_c are (7.6 ± 0.2), (7.8 ± 0.2), and (8.1 ± 0.2) MeV, respectively.

It should be noted that in some papers the term «critical temperature» is not used in the strict thermodynamic sense given above. In Ref. [64] multifragmentation in $\mathrm{Au} + \mathrm{Au}$ collisions at 35 MeV per nucleon was analyzed with the so-called Campi plot [61] to prove that the phase transition takes place in the spinodal region. The characteristic temperature for that process was denoted as T_{crit} and found to be equal to (6.0 ± 0.4) MeV. In Ref. [114] the bond percolation

model is used to interpret fragment emission in 10.2 GeV/c $p + \mathrm{Au}$ collisions. The critical value of the percolation parameter $p_c = 0.65$ was found from the analysis of the IMF charge distribution. The corresponding «critical temperature» of (8.3 ± 0.2) MeV is estimated by using the model relation between the percolation control parameter and the excitation energy. The more appropriate term here is the «break-up temperature». This temperature corresponds to the onset of the fragmentation of the nucleus entering the phase coexistence region. Sometimes the term «limiting temperature» is used also for that. Analysis of the experimental data on the «limiting temperatures» was used to derive T_c of the neutral nuclear matter, which was found to be equal to (16.6 ± 0.86) MeV [115].

There is only one paper in which T_c is estimated by using data other than the fragmentation ones. In Ref. [116] it is done by the analysis of the temperature dependence of the fission probability. It is considered in the next section.

Having in mind the shortcomings of Fisher's model [99, 117], we have estimated the nuclear critical temperature in the framework of the statistical model, SMM, as it describes well the different properties of the thermal multifragmentation of target spectators produced in collisions by light relativistic ions. Results are given in Subsec. 3.3.

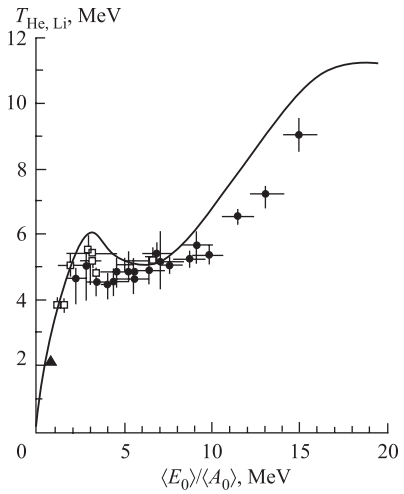

Fig. 30. Temperature as a function of the excitation energy. The experimental data are mainly from [118], the lowest value of T is taken from Ref. [107]. The line is calculated for the fragmenting nucleus with mass number $A_0 = 100$ in [34] with statistical model of multifragmentation SMM

3.2. Critical Temperature from the Analysis of the Fission Probabilities. This subsection is given following to [116]. This study was stimulated by the paper of Pochodzalla et al. [118], in which the first caloric curve was measured for the system created in $\mathrm{Au} + \mathrm{Au}$ collisions at 600 MeV/nucleon (Fig. 30). The observed plateau was interpreted as a signature of the liquid–gas phase transition with the critical temperature $T_c \approx 5$ MeV.

The use of the experimental data on fission probabilities for the estimation of the critical temperature, T_c, has an obvious motivation. The fissility of heavy nuclei is determined by the ratio of the Coulomb and surface free energies: the larger the ratio, the smaller the fission barrier. The surface tension *vanishes at the critical temperature*. As temperature approaches the critical one from below, the surface tension (and surface energy) gradually decreases, fission barrier becomes lower. Thus, the measurement of fission prob-

abilities as a function of the excitation energy gives a chance to estimate how far the system is from the critical point. Temperature effects in the fission barrier have been considered in a number of theoretical studies based on different models (see, e.g., Ref. [109, 119–124]. The effect is so large for hot nuclei that the barrier vanishes at temperatures of 4–6 MeV for the critical temperature T_c being in the range 15–18 MeV.

In terms of the standard liquid–drop conventions [125], the fission barrier can be represented as a function of temperature by the following relation:

$$B_f(T) = E_s(T_s) - E_s^0(T) + E_c(T_s) - E_c^0(T) = \\ = E_s^0(T)[(B_s - 1) + 2x(T)(B_c - 1)], \quad (8)$$

where B_s is the surface (free) energy at the saddle point, $E_s(T_s)$, in units of surface energy $E_s^0(T)$ of a spherical drop; B_c is the Coulomb energy $E_c(T_s)$ at the saddle deformation in units of Coulomb energy $E_c^0(T)$ of the spherical nucleus. For the surface energy and the fissility parameter $x(T)$, one can write [119]:

$$E_s^0(T) = E_s^0(0)\sigma(T)/\sigma(0)[\rho(0)/\rho(T)]^{2/3}, \\ x(T) = \frac{E_c^0(T)}{2E_s^0(T)} = x(0)\frac{\rho(T)\sigma(0)}{\rho(0)\sigma(T)}, \quad (9)$$

where $\sigma(T)$ and $\rho(T)$ are the surface tension and the mean nuclear density for a given temperature. As a first approximation, we neglect the difference between the temperature at the saddle T_s and T. In that case the values B_s and B_c are determined by the deformation at the saddle point, which depends on the fissility parameter $x(T)$.These quantities were tabulated by Nix [125] for the full range of the fissility parameter. For $\sigma(T)$ we use the approximation:

$$\sigma(T) = \sigma(0)\left[\frac{T_c^2 - T^2}{T_c^2 + T^2}\right]^{5/4}. \quad (10)$$

This equation was obtained in Ref. [126], devoted to the theoretical study of thermodynamic properties of a plane interface between two phases of nuclear matter (liquid and gas) in equilibrium. This parameterization is successfully used by the SMM for describing the multifragment decay of hot finite nuclei. In accordance with [125], the expressions for $E_s^0(0)$ and $x(0)$ are taken to be

$$E_s^0(0) = 17.94\gamma A^{2/3}\ \text{MeV}, \quad x(0) = \frac{Z^2/A}{50.88\gamma}, \\ \gamma = 1{-}1.7826[(N - Z)/A]^2. \quad (11)$$

Sauer et al. [109] investigated the thermal properties of nuclei by using the Hartree–Fock approximation with the Skyrme force. The equation of the state was obtained which gives the critical temperature $T_c \approx 18$ MeV for finite nuclei. In this case the temperature dependence of the mean nuclear density is found to be $\rho(T) = \rho(0)(l - \alpha T^2)$, where $\alpha = 1.26 \cdot 10^{-3}$ MeV^{-2}. If the value of T_c has another value, the parameter «α» also takes a different value. We assume that α is proportional to T_c^{-2}, as like as in the case of $\sigma(T)$ for $T \ll T_c$. Using the results of [109], one obtains:

$$\rho(T) = \rho(0)(l - 0.4T^2/T_c^2). \tag{12}$$

Figure 31 shows the relative values of $\sigma(T)$, $\rho(T)$, and $x(T)$ as a function of T/T_c. A drastic change of nuclear fissility is expected even halfway to the critical point. Figure 32 displays the calculated liquid–drop fission barrier for ^{188}Os as a function of temperature. Virtually, it vanishes for $T > 0.4T_c$. This nucleus has been chosen since the results of the calculations can be compared with the experimental data for it for temperatures up to 2.5 MeV.

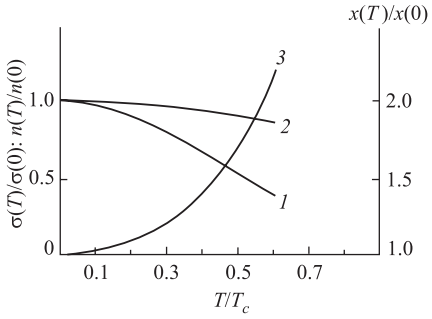

Fig. 31. Relative values of the surface tension (*1*), mean nuclear density (*2*), and fissility parameter (*3*) as a function of temperature in the units of critical one

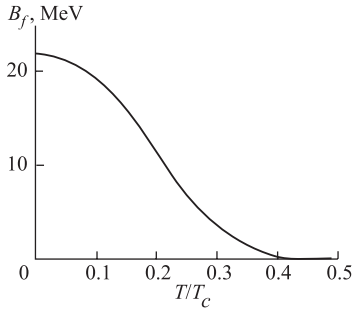

Fig. 32. Temperature dependence of liquid–drop fission barrier for ^{188}Os

To estimate the fission and evaporation rates, the statistical model is used. The first-chance fission probability $\Gamma_f/(\Gamma_f + \Gamma_n)$ is calculated by the Moretto relation [127]

$$\frac{\Gamma_f}{\Gamma_n} = \frac{\pi\hbar^2}{4m\sigma_{\rm CN}} \frac{T_s}{T_R^2} \frac{\omega_s(E - B_f)}{\omega_R(E - B_n)}, \tag{13}$$

where ω_s is the level density at the saddle point; ω_R and T_R are the level density and the temperature of the residual nucleus (after neutron emission); m and $\sigma_{\rm CN}$ are the neutron mass and the capture cross section. For the level density the expression from the Fermi-gas model is used [128].

Figure 33 presents the results of calculations of the fission probabilities for ^{188}Os assuming $T_c = 5$ MeV and $T_c = 10$ MeV as a function of the excitation energy. We restricted ourselves to the temperature range 2–2.5 MeV, as the calculations were made under the assumption, that $T_s \approx T$. In this temperature range, the fission barrier is close to zero for $T_c = 5$ MeV and less than 11 MeV for $T_c = 10$ MeV. The experimental data for fission in $^4\mathrm{He} + {}^{184}\mathrm{W}$ collisions are taken from Ref. [129]. The curve passing through the points is a result of theoretical fit made in [129] with the fission barrier $B_f = 24.2$ MeV corrected for the shell effects.

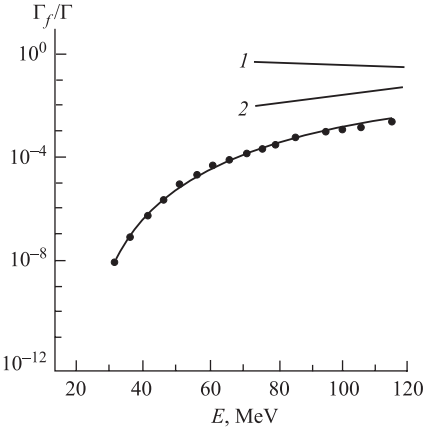

Fig. 33. Fission probabilities of ^{188}Os. The experimental data are from [129]. The upper lines are calculated for $T_c = 5$ MeV (*1*) and 10 MeV (*2*)

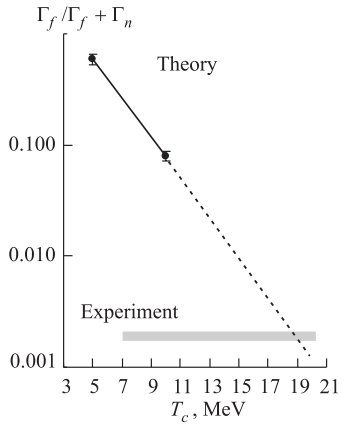

Fig. 34. Fission probabilities for ^{188}Os at excitation energy 117 MeV. The calculated values are given as a function of the assumed critical temperature. Extrapolation of calculated values to the measured one gives $T_c = (19 \pm 3)$ MeV

The comparison of the experimental data and calculations definitely exclude $T_c = 5$ MeV and $T_c = 10$ MeV. Thus, critical temperature for the liquid–gas phase transition in nuclear media is *larger* than 10 MeV. In Ref. [116], we did not perform the calculation of fission probabilities with higher values of T_c because of the restrictions of the formalism used. Figure 34 shows extrapolation of the calculated fission widths to the larger values of critical temperatures. As a result, one gets: $T_c = (19 \pm 3)$ MeV. The error bar takes into account the estimated accuracy of the model used.

3.3. Critical Temperature from the IMF Charge Distribution. In this analysis the statistical model of multifragmentation, SMM, was used. Within this model one considers a microcanonical ensemble of all break-up channels

composed of nucleons and excited fragments of different masses. It is assumed that an excited nucleus expands to a certain volume and then breaks up into nucleons and hot fragments. It is also assumed that fragmenting nucleus is in thermal equilibrium, characterized by the channel temperature T determined from the energy balance. The probability W_j of a decay channel j is proportional to its statistical weight:

$$W_j \sim \exp\, S_j(E_x, A_0, Z_0), \tag{14}$$

where S_j is the entropy of the system in a state corresponding to the decay channel j. The excitation energy, mass, and charge of the decaying system are denoted by E_x, A_0, and Z_0, respectively. The fragments with mass numbers $A > 4$ are treated as heated nuclear liquid drops.

Channels are characterized by the multiplicities, N_{AZ}, of fragments ${}^{A}Z$. The channel entropy is obtained by summing the entropies of all the particles in a given channel:

$$S_j = \sum N_{AZ} S_{AZ}, \quad S_{AZ} = -\left(\frac{\partial F_{AZ}}{\partial T}\right)_V. \tag{15}$$

The fragment free energy F_{AZ} is a sum of volume, surface, symmetry, Coulomb and translational terms:

$$F_{AZ} = F^V_{AZ} + F^S_{AZ} + F^{\rm sym}_{AZ} + F^C_{AZ} + F^t_{AZ}. \tag{16}$$

The surface energy term, F^S_{AZ}, depends upon the critical temperature, so the fragment charge distribution is sensitive to the value of T_c, as the surface tension coefficient depends on T/T_c. The following expression is used in the SMM for F^S_{AZ}:

$$F^S_{AZ} = a_s(T) A^{2/3}, \quad a_s(T) = a_s(0)\left(\frac{T_c^2 - T^2}{T_c^2 + T^2}\right)^{5/4}, \tag{17}$$

with $a_s(T) = 4\pi r_0^2 \sigma(T)$, where $\sigma(T)$ is a temperature-dependent coefficient of the surface tension according to Eq. (9). Figure 35 shows $a_s(T)/a_s(0)$ as a function of T/T_c. The symbols are taken from the calculations of Ref. [109], which was made in different manner comparing to [126]. Agreement of so different calculations is in a favor of reliability of Eq. (17). Two other parameterizations of $\sigma(T)$ are presented also: linear one $\sim (1 - T/T_c)$, which is used in the analysis with Fisher droplet model [112–114], and quadratic one $\sim (1 - T/T_c)^2$ [23]. *The comparison of the measured and calculated fragment charge distributions is the way to estimate the critical temperature* T_c. It has been done in the framework of SMM in Refs. [130, 131] by the analysis of the data for $p + \mathrm{Au}$ collisions at 8.1 and 3.6 GeV obtained by FASA collaboration.

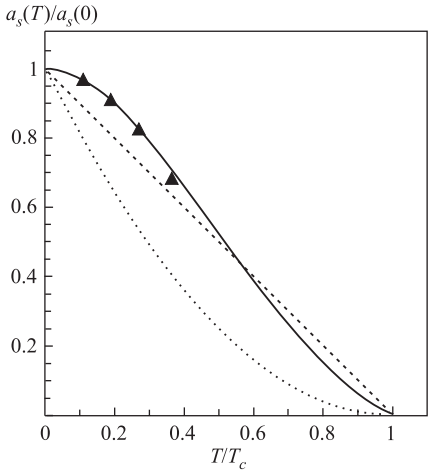

Fig. 35. The calculated temperature-dependent coefficient of the surface tension as a function of T/T_c: solid line is according to Eq. (17), dashed and dotted lines are for linear and quadratic parameterizations of $a_s(T)/a_s(0)$ as a function of T/T_c

As is already written above, the reaction mechanism for the light relativistic projectiles is usually divided into two stages. The first one is a fast energy-depositing stage, during which very energetic light particles are emitted and a nuclear remnant is excited. We use the intranuclear cascade model (INC) [32] for describing this stage. The second stage is described by the SMM, which considers multibody decay of a hot and expanded nucleus. But such a two-stage approach fails to explain the observed IMF multiplicities. An expansion stage (Exp.) is inserted between the two parts of the calculation. The excitation energies and the residual masses are fine tuned [12] to get agreement with the measured IMF multiplicities, i.e., the values for the residual (after INC) masses and their excitation energies are scaled on an event-by-event basis.

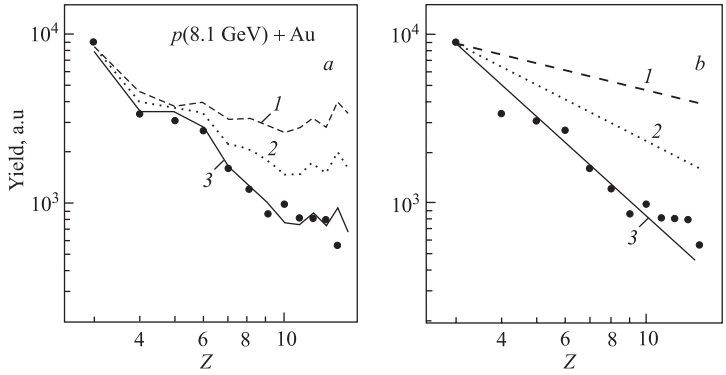

Fig. 36. The measured (dots) and calculated fragment charge distributions for $p + \mathrm{Au}$ at 8.1 GeV: *a*) the lines are calculated with INC + Exp. + SMM model, assuming $T_c = 7$ (*1*), 11 (*2*), and 18 MeV (*3*); *b*) the power-law fits

Figure 36, *a* presents the measured fragment charge distribution for $p(8.1\ \mathrm{GeV}) + \mathrm{Au}$ collisions and the calculations performed with T_c as a free parameter. For all values of T_c the calculations with the INC + Exp. + SMM

model have been properly adjusted to get the mean IMF multiplicity close to the measured one. The lines show the calculated charge distributions for $T_c = 7$, 11, and 18 MeV using Eq. (17). Very important SMM parameter k is taken to be $k = 2$. It corresponds to the break up density $\rho_t = 1/3\rho_0$. A level density parameter is taken to be equal to $a = A/8$. The statistical errors of the measurements do not exceed the size of the dots. The data are corrected for the counting rate loss caused by the cutoff (~ 1.2 MeV/nucleon) in the low-energy part of the IMF spectra. The correction is the largest ($\sim 15\%$) for the heavier IMFs. The calculations are close to the data for $T_c = 18$ MeV. The estimated mean temperature of the fragmenting system is around 6 MeV, the mean charge and mass numbers are 67 and 158, respectively. The theoretical curve deviates from the data with decreasing T_c. Figure 36, *b* gives the results of the power-law fits for the data and model calculations. In Ref. [131] it was done for the range of $Z = 4{-}11$: Li-fragments were excluded to illuminate the contribution of the pre-equilibrium emission. The yield of Be was corrected in the fitting procedure for the loss of unstable ^{8}Be. Similar results are obtained for $p + \mathrm{Au}$ collisions at 3.6 GeV.

Comparisons of the experimental power-law exponents (for both proton energies) and model predicted ones for different assumed values of T_c are presented in Fig. 37, *a*, *b*. The measured power-law exponents are given as a band with a width determined by the statistical error. The size of the symbols for the calculated values of τ_{app} exceeds the error bar. Following to [96], we use the term «apparent power-law exponent» having in mind that power-law describes the data only approximately sometimes. From the best fit of calculations to the data one concludes that critical temperature is

$$T_c = (17 \pm 2) \text{ MeV}$$

for both beam energies. This value is 15% smaller than T_c estimated in our previous paper [130], in which the experimental value of τ_{app} was found by the fitting in the range of $Z = 3{-}11$. The contribution of the pre-equilibrium emission resulted in some increasing of the apparent exponent and overestimation of the critical temperature.

The calculations have been performed also using the surface tension coefficient linearly dependent on T/T_c as like as in Refs. [112–114]. It was done for $p + \mathrm{Au}$ collisions at 8.1 GeV. The calculated values of τ_{app} in this case are remarkably lower than the measured one (Fig. 37, *b*). Similar results have been obtained for the quadratic parameterization of $a_s(T)/a_s(0)$. It can be considered as an indication that these parameterizations are not adequate.

It has been checked how results are sensitive to the level density parameter, having in mind that the IMF charge distribution is very much influenced by the secondary decay of hot primary fragments. The calculations with $a = A/10$ are

shown in Fig. 37, *c*: the curves are only slightly changed. The lower line in Fig. 37 is obtained under assumption of $k = 5$, which corresponds to the mean density of the system at fragment formation stage equal to $\rho_t = 1/6\rho_0$. Calculated values of the power-law exponent are remarkably below the measured one at any value of critical temperature assumed. This result is consistent with conclusions given in Subsec. 2.2.1.

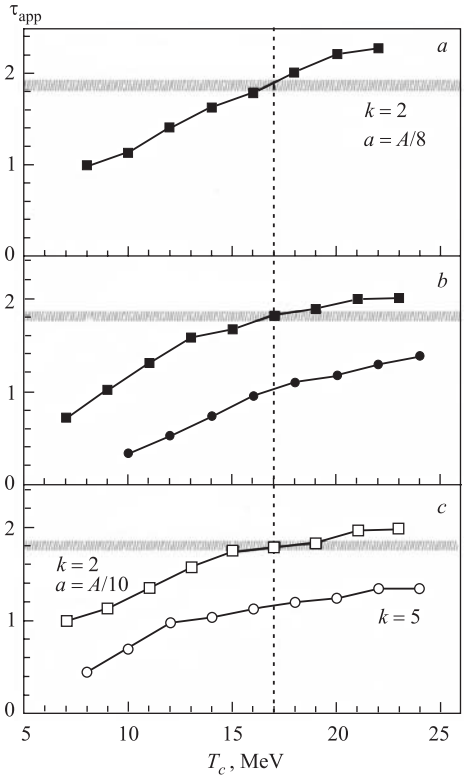

Fig. 37. Power-law exponents for the IMF's charge distributions for $p + \mathrm{Au}$ collisions at 3.6 (*a*) and 8.1 GeV (*b*, *c*). The bands correspond to the measured values and their error bars. *a*, *b*) Solid squares are obtained by calculations using Eq. (17) for different values of T_c; break-up density, ρ_t, is taken to be 1/3 ρ_0, level density parameter a is $A/8$; solid circles are calculated for the linear dependence of the surface tension on T/T_c. *c*) Open squares are obtained for a reduced value of level density parameter, open circles are calculated under assumption of a more dilute fragmenting nucleus ($\rho_t = 1/6\rho_0$). The best fit of calculations and data corresponds to $T_c = (17 \pm 2)$ MeV

The obtained value of the critical temperature should be considered as some effective value averaged over all the fragments produced in the collision. This value is significantly larger than those found in [112–114] by the analysis of the multifragmentation data in terms of Fisher's droplet formalism. Although our value for T_c is model-dependent, as is any other estimate of the critical temperature, the analysis presented here provides strong support for a value of $T_c > 15$ MeV for finite nuclei. One can say that it is illusive to imagine the nucleus at so high temperature. It is right! But nuclear (or nucleon) systems do exist even at higher temperatures, e.g., nuclear fire-balls in high-energy nucleus–nucleus collisions. Virtually, critical temperature T_c is a parameter, which determines how fast the surface tension is decreasing with nucleus heating.

Some general consideration of the problem of the critical temperature in the framework of SMM is given in [132].

3.4. Spinodal Decomposition as a Nuclear Liquid–Fog Phase Transition. Figure 38 presents the proposed phase unstable region (spinodal one, according to [109]) with the experimental data obtained for $p(8.1\ \mathrm{GeV}) + \mathrm{Au}$ collisions by FASA collaboration. The points for the partition and freeze-out configurations are located at ρ_t and ρ_f [78]. Corresponding temperatures have been determined by fitting the data for fragment yields with the statistical model calculations [73]. The estimated value of the fragmentation barrier has been taken into account. These two points (at ρ_t and ρ_f) are deep inside the spinodal region, the top of which is specified by the critical temperature for the liquid–gas phase transition [131]. These observations give a good basis for the interpretation of multifragmentation phenomenon as spinodal decomposition of hot nuclei, which can be considered as a first order phase transition, when the structure of the nuclear substance is changing very fast and drastically. Very short fragment emission time is in accordance with this scenario. It should be noted that configuration at mean density ρ_f does belong to the spinodal region although it consists of the fragments at normal density inside the freeze-out volume.

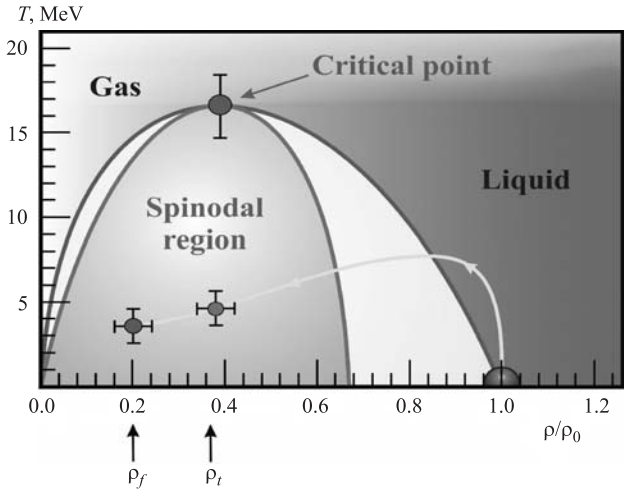

Fig. 38. Proposed spinodal region for nuclear system. The experimental points were obtained by the FASA collaboration. The arrow line shows the way of the system from the starting point at $T = 0$ and $\rho = \rho_0$ to the multiscission point at ρ_f

The spinodal decomposition as a key mechanism of nuclear multifragmentation has been considered in a number of papers (see, for example [24, 97, 133–138]). In some papers, the peculiar signals of the first order phase transition

were looked for among the observables of the multifragment emission process. First of all, it is the observation of the plateau in the shape of caloric curve by ALADIN collaboration [118] followed by the stream of papers by other groups (e.g., [139]). The flattering caloric curve is interpreted as a result of latent heat in the phase transition. The similarity to the boiling process of ordinary liquid has been noted many times. But it should be stressed that boiling does not take place inside the spinodal region.

Other signals of the phase transition have been considered also: a) energy fluctuations from event to event (negative heat capacity) [65, 136, 140, 141]; b) fluctuations in the partition process (Campi-plot) [61, 64]; c) bimodality of the probability distributions of the observable quantities [142, 143]; d) enhanced production of equal-sized fragments as a fossil signature of spinodal decomposition [24].

Theoretical activity in this field [19, 23, 62, 111, 144–146] has been very impressive in demonstration, that multifragment emission is the result of «*real phase transition in finite nuclei in its proper statistical or thermodynamical meaning*» (D. H. E. Gross).

How to call it? It is clear for us, that it is not nuclear liquid–gas phase transition. Obvious rule is to use the names of the initial and final states. No questions are about the initial phase, it is nuclear liquid. As for the final state, it is not a gas, it is nuclear fog. So, the proper name is nuclear *liquid–fog* phase transition [116]. The use of this term was motivated already in 1984 by Siemens [108]. One year later another term was suggested by Bondorf et al. [34] — «cracking» phase transition. It is used rather seldom now, and that is reasonable, as «cracking» is the process, but not the final state of transition. The final state is the droplets (intermediate mass fragments) surrounded by nuclear gas, i.e., nuclear fog. The classical fog is unstable substance, which transforms finally into liquid «sea» with «atmosphere» of the saturated vapor. The nuclear, charged fog is stable in respect to such fortune. But it «explodes» because of the Coulomb repulsion. This event is detected as multifragmentation.

What is the place of the phase transitions considered above in the general nuclear phase diagram? It is presented in Fig. 39 as designed twenty years ago by Goodman et al. [62, 147]. The region of spinodal decomposition (liquid–fog phase transition) is shown in the left corner. Now the contour of this region is checked experimentally.

Let us go to the nuclear matter, which is more compressed than the ordinary one. At the densities ρ/ρ_0 larger than 3 and temperatures up to several tens of MeV, a very exotic phase is predicted in [148–150], which is called «π condensate». Here, nuclear matter is like a crystal, which has spin–isospin ordered structure. Many efforts to find any experimental indication on that were unsuccessful [151]. The interior of the neutron stars might be composed of π-condensed matter.

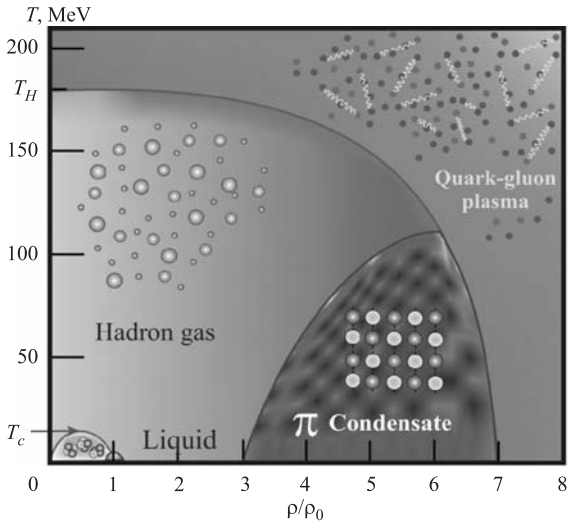

Fig. 39. Proposed nuclear phase diagram: ρ/ρ_0 is the baryon density in the units of the normal nuclear density, the spinodal region is shown in the lower left corner

At higher densities and temperatures, the phase transition to quark matter (or quark–gluon plasma) is predicted. Here, quarks should be no longer confined within hadrons. The resultant phase is a hot gas of quarks, which are exchanging by gluons. The unique signal of formation of this state is abnormal suppression of the J/ψ production in the very relativistic heavy ion collisions. In 1988, it was claimed that effect had been observed in collisions $^{16}\mathrm{O}$ (200 GeV/A) + $^{38}\mathrm{U}$ [152]. Later, this conclusion was canceled. It was understood that detecteded suppression was caused by J/ψ absorption in the target nuclear matter. The recent analysis [153] shows that some additional suppression of J/ψ yield is still observed for the central $\mathrm{Pb} + \mathrm{Pb}$ collisions at 158 GeV/A, which is interpreted as a signal of creation of a new state of matter. Thus, twenty years of tremendous efforts of several hundreds of scientists did not result in unambiguous discovery of the quark matter.

Significance of the liquid–fog and liquid–gas phase transitions for nuclear physics is evident, though it may be not as fundamental as the transition to quark–gluon plasma. However, it *does definitely exist*! Moreover, its investigation may be useful for understanding the supernova dynamics as it is demonstrated in recent papers [154, 155].

Acknowledgements. The author is thankful to Drs. S. P. Avdeyev, O. V. Bochkarev, A. S. Botvina, A. Budzanowski, L. V. Chulkov, M. Janicki, W. Karcz, V. V. Kirakosyan, E. A. Kuzmin, F. Lips, E. Norbeck, H. Oeschler,

V. K. Rodionov, P. A. Rukoyatkin, A. V. Simonenko, I. Skwirczynska for collaboration in FASA project for many years. We are remembering heartily G. B. Jan'kov and L. A. Petrov, who left us so early.

The author is grateful to A. Hrynkiewicz, A. I. Malakhov, A. G. Olchevsky, and A. N. Sissakian for support. This work was supported in part by the Russian Foundation for Basic Research, Grant No. 06-02-16068 and by the Grant of the Polish Plenipotentiary to JINR.

REFERENCES

1. *Gurevich I. I. et al.* // Dokl. AN SSSR. 1938. V. 18. P. 169.
2. *Schopper E.* // Naturwissenschaftler. 1937. Bd. 5. S. 557.
3. *Lozhkin O. V., Perfilov N. A.* // Zh. Eksp. Teor. Fiz. 1956. V. 31. P. 913.
4. *Perfilov N. A., Lozkin O. V., Shamov V. P.* // Sov. Phys. Usp. 1960. V. 38. P. 345.
5. *Jakobsson B. et al.* // Z. Phys. A. 1982. V. 307. P. 293.
6. *Siemens P. J.* // Nature. 1983. V. 305. P. 410.
7. *Finn J. E. et al.* // Phys. Rev. Lett. 1982. V. 49. P. 1321.
8. *Hirsh A. S. et al.* // Phys. Rev. C. 1984. V. 29. P. 508.
9. *Avdeichikov et al.* // Yad. Fiz. 1988. V. 48. P. 1736.
10. *Murata J.* PhD Thesis. KEK, Japan, Tsukuba, 1999.
11. *Desbois J. et al.* // Z. Phys. A. 1987. V. 328. P. 101.
12. *Avdeyev S. P. et al.* // Eur. J. Phys. A. 1998. V. 3. P. 75.
13. *De Paula L. et al.* // Phys. Lett. B. 1991. V. 258. P. 251.
14. *Hüfner J.* // Phys. Rep. 1985. V. 125. P. 129.
15. *Lynch W. G.* // Ann. Rev. Nucl. Part. Sci. 1987. V. 37. P. 493.
16. *Moretto L. G., Wozniak G. J.* // Ann. Rev. Nucl. Part. Sci. 1993. V. 44. P. 379; *Moretto L. G. et al.* // Phys. Rep. 1997. V. 287. P. 249.
17. *Guerreau D.* // Nucl. Phys. A. 1994. V. 574. P. 111c.
18. *Cugnon J.* // Yad. Fiz. 1994. V. 57. P. 1705.
19. *Bondorf J. et al.* // Phys. Rep. 1995. V. 257. P. 133.
20. *Gross D. H. E.* // Phys. Rep. 1997. V. 279. P. 119.
21. *Tamain B., Duraund D.* // Session LXVI. Les Houches. Amsterdam, 1998. P. 295.
22. *Bonasera A. et al.* // Rivista del Nuovo Cim. 2000. V. 23. P. 1.
23. *Richert J., Wagner P.* // Phys. Rep. 2001. V. 350. P. 1.
24. *Borderie B.* // J. Phys. G: Nucl. Part. Phys. 2002. V. 28. P. R217.
25. *Chomaz P., Colonna M., Randrup J.* // Phys. Rep. 2004. V. 389. P. 263.
26. *Napolitani P. et al.* // Phys. Rev. C. 2004. V. 70. P. 054607.
27. *Karnaukhov V. A. et al.* // Yad. Fiz. 1999. V. 62. P. 272.
28. *Avdeyev S. P. et al.* // Phys. At. Nucl. 2001. V. 64. P. 1549; Phys. Lett. B. 2001. V. 503. P. 256.

29. *Avdeyev S. P. et al.* // Nucl. Phys. A. 2002. V. 709. P. 392.
30. *Avdeyev S. P. et al.* // Nucl. Instr. Meth. A. 1993. V. 332. P. 149.
31. *Avdeyev S. P. et al.* // Prib. i Tekhn. Eksp. 1996. V. 39. P. 7; Instr. Exp. Techn. 1996. V. 39. P. 153.
32. *Toneev V. D. et al.* // Nucl. Phys. A. 1990. V. 519. P. 463c.
33. *Amelin N. S. et al.* // Yad. Fiz. 1990. V. 52. P. 272.
34. *Bondorf J. P. et al.* // Nucl. Phys. A. 1985. V. 443. P. 321; V. 444. P. 460.
35. *Botvina A. S. et al.* // Yad. Fiz. 1985. V. 42. P. 1127.
36. *Gross D. H. E.* // Rep. Progr. Phys. 1990. V. 53. P. 605.
37. *Konopka J. et al.* // Phys. Rev. C. 1994. V. 50. P. 2085.
38. *Randrup J.* // Comp. Phys. Commun. 1993. V. 77. P. 153.
39. *Toke J., Jun Lu, Schröder W. U.* // Phys. Rev. C. 2003. V. 67. P. 034609;
Toke J., Jun Lu, Schröder W. U. // Ibid. P. 044307.
40. *Sobotka L. G. et al.* // Phys. Rev. Lett. 2004. V. 93. P. 132702.
41. *Friedman W. A.* // Phys. Rev. C. 1990. V. 42. P. 667.
42. *Avdeyev S. P. et al.* // JINR Rapid Commun. 1997. No. 2[82]. P. 71.
43. *Foxford E. R. et al.* // Phys. Rev. C. 1996. V. 54. P. 749;
Moreley K. B. et al. // Ibid. P. 737.
44. *Schüttauf A. et al.* // Nucl. Phys. A. 1996. V. 607. P. 457.
45. *Hsi W. C. et al.* // Phys. Rev. Lett. 1994. V. 73. P. 3367;
Kunde G. J. et al. // Phys. Rev. Lett. 1995. V. 74. P. 38.
46. *Trockel R. et al.* // Phys. Rev. C. 1989. V. 39. P. 729.
47. *de Souza R. T. et al.* // Phys. Lett. B. 1991. V. 268. P. 6.
48. *Bowmann D. R. et al.* // Phys. Rev. C. 1992. V. 46. P. 1834.
49. *Jacak B. V.* // Nucl. Phys. A. 1988. V. 488. P. 325c.
50. *Baden A. et al.* // Nucl. Instr. Meth. A. 1982. V. 203. P. 189.
51. *Reisdorf W. et al.* // Nucl. Phys. A. 1997. V. 612. P. 493.
52. *Shmakov S. Yu. et al.* // Phys. At. Nucl. 1995. V. 58. P. 1635.
53. *de Souza R. T. et al.* // Phys. Lett. B. 1993. V. 300. P. 29.
54. *Jeong S. C. et al.* // Phys. Rev. Lett. 1994. V. 72. P. 3468.
55. *Lips V. et al.* // Phys. Lett. B. 1994. V. 338. P. 141.
56. *Ogilve C. et al.* // Phys. Rev. Lett. 1991. V. 67. P. 1214.
57. *ALADIN Collab.* GSI Report. 1989. 02-89.
58. *Milkau U. et al.* // Phys. Rev. C. 1991. V. 44. P. R1242.
59. *Milkau U. et al.* // Z. Phys. A. 1993. V. 346. P. 277.
60. *Lefort T. et al.* // Phys. Rev. C. 2001. V. 64. P. 064603.
61. *Campi X.* // Nucl. Phys. A. 1989. V. 495. P. 259c.
62. *Goodman A. L., Kapusta J. I., Mekjian A. Z.* // Phys. Rev. C. 1984. V. 30. P. 851.
63. *Vient E. et al.* // Nucl. Phys. A. 2002. V. 700. P. 535.

64. *D'Agostino M. et al.* // Nucl. Phys. A. 1999. V. 650. P. 329.
65. *D'Agostino M. et al.* // Nucl. Phys. A. 2002. V. 699. P. 795.
66. *Beaulieu L. et al.* // Phys. Lett. B. 1999. V. 463. P. 159.
67. *Lefort T. et al.* // Phys. Rev. C. 2000. V. 62. P. 031604.
68. *J Gosset et al.* // Phys. Rev. C. 1977. V. 16. P. 629.
69. *Shapiro O., Gross D. H. E.* // Nucl. Phys. A. 1994. V. 573. P. 143.
70. *Bowman D. R. et al.* // Phys. Rev. C. 1995. V. 52. P. 818.
71. *Wang G. et al.* // Phys. Rev. C. 1998. V. 57. P. R2786.
72. *Beaulieu L. et al.* // Phys. Rev. Lett. 2000. V. 84. P. 5971.
73. *Rodionov V. K. et al.* // Nucl. Phys. A. 2002. V. 700. P. 457.
74. *Durand D.* // Nucl. Phys. A. 1998. V. 630. P. 52c.
75. *Bao-An Li et al.* // Phys. Lett. B. 1994. V. 335. P. 1.
76. *Bracken D. S. et al.* // Phys. Rev. C. 2004. V. 69. P. 034612.
77. *Karnaukhov V. A. et al.* // Ibid. V. 70. P. 041601(R).
78. *Karnaukhov V. A. et al.* // Nucl. Phys. A. 2005. V. 749. P. 65c.
79. *Oeschler H. et al.* // Part. Nucl., Lett. 2000. No. 2[99]. P. 70.
80. *Natowitz J. B. et al.* // Phys. Rev. C. 2002. V. 66. P. 031601(R).
81. *Lopez J. A., Randrup J.* // Nucl. Phys. A. 1989. V. 503. P. 183; 1990. V. 512. P. 345.
82. *Campi X. et al.* // Phys. Rev. C. 2003. V. 67. P. 044610.
83. *Dorso C., Randrup J.* // Phys. Lett. B. 1993. V. 301. P. 328.
84. *Srachan A., Dorso C.* // Phys. Rev. C. 1997. V. 55. P. 775.
85. *Dorso C. et al.* // Phys. Rev. C. 2004. V. 69. P. 034610.
86. *Cassing W.* // Z. Phys. A. 1987. V. 327. P. 447.
87. *Borderie B.* Preprint Orsay/IPNO-DRE-92-03.
88. *Curtin M. W., Toki H., Scott D. K.* // Phys. Lett. B. 1983. V. 123. P. 289.
89. *Wang G. et al.* // Phys. Rev. C. 1996. V. 53. P. 1811.
90. *Norenberg W., Papp G., Rozmej P.* // Eur. Phys. J. A. 2002. V. 14. P. 43.
91. *Baran V. et al.* // Nucl. Phys. A. 2002. V. 703. P. 603.
92. *Goldenbaum F. et al.* // Phys. Rev. C. 1999. V. 82. P. 5012;
Karamyan A. S. et al. // Eur. Phys. J. A. 2003. V. 17. P. 49.
93. *Odeh T. et al.* // Phys. Rev. Lett. 2000. V. 84. P. 4557.
94. *Hilscher D., Rosner H.* // Ann. de Phys. 1992. V. 17. P. 471.
95. *Brosa U. et al.* // Phys. Rep. 1990. V. 197. P. 162.
96. *Panagiotou A. D. et al.* // Phys. Rev. C. 1985. V. 31. P. 55.
97. *Porile N. T. et al.* // Phys. Rev. C. 1989. V. 39. P.1914.
98. *Fisher M. E.* // Physics. 1967. V. 3. P. 255.
99. *Schmelzer J., Roepke G., Ludwig F.* // Phys. Rev. C. 1997. V. 55. P.1917.

100. *Tanaka K. H. et al.* // Nucl. Phys. A. 1995. V. 583. P. 581;
Murakami T. et al. // Proc. of the 10th Conf. on Nucl. Reac. Mech., Varenna, 2003, Universita degli study di Milano. Suppl. No. 122. P. 541.

101. *Remsberg L. P., Perry D. G.* // Phys. Rev. Lett. 1975. V. 35. P. 361.

102. *Fortney D. R., Porile N. T.* // Phys. Lett. B. 1978. V. 76. P. 553.

103. *Urbon J. et al.* // Phys. Rev. C. 1980. V. 21. P. 1048.

104. *Gudima K. K., Toneev V. D.* // Phys. Lett. B. 1978. V. 73. P. 293.

105. *Hsi W.-C. et al.* // Phys. Rev. C. 1998. V. 58. P. R13.

106. *Jaqaman H., Mekjian A. Z., Zamick L.* // Phys. Rev. C. 1983. V. 27. P. 2782.

107. *Borcea C. et al.* // Nucl. Phys. A. 1984. V. 415. P. 169.

108. *Siemens P. J.* // Ibid. V. 428. P. 189c.

109. *Sauer G., Chandra H., Mosel U.* // Nucl. Phys. A. 1976. V. 264. P. 221.

110. *Zhang Feng Shou* // Z. Phys. A. 1996. V. 356.

111. *Taras S. et al.* // Phys. Rev. C. 2004. V. 69. P. 014602.

112. *Elliott J. B. et al.* // Phys. Rev. Lett. 2002. V. 88. P. 042701.

113. *Elliott J. B. et al.* // Phys. Rev. C. 2003. V. 67. P. 024609.

114. *Kleine Berkenbusch M. et al.* // Phys. Rev. Lett. 2002. V. 88. P. 022701.

115. *Natowitz J. et al.* // Ibid. V. 89. P. 212701.

116. *Karnaukhov V. A.* // Phys. At. Nucl. 1997. V. 60. P.1625.

117. *Reuter P. T., Bugaev K. A.* // Phys. Lett. B. 2001. V. 517. P. 233.

118. *Pochodzalla J. et al.* // Phys. Rev. Lett. 1995. V. 75. P. 1040.

119. *Hasse R. W., Stocker W.* // Phys. Lett. B. 1973. V. 44. P. 26.

120. *Iljinov A. S. et al.* // Z. Phys. A. 1978. V. 287. P. 37.

121. *Pi M. et al.* // Phys. Rev. C. 1982. V. 26. P. 773.

122. *Bartel J., Quentin P.* // Phys. Lett. B. 1985. V. 152. P. 29.

123. *Brack M. et al.* // Phys. Rep. 1985. V. 123. P. 275.

124. *Garcias F. et al.* // Z. Phys. A: At. Nucl. 1990. V. 336. P. 31.

125. *Nix J.* // Nucl. Phys. A. 1968. V. 130. P. 241.

126. *Ravenhall D. G. et al.* // Nucl. Phys. A. 1983. V. 407. P. 571.

127. *Moretto L. G.* // Proc. of the 3rd Symp. Phys. Chem. of Fission, Rochester, N. Y., 1973. Vienna, 1974. V. 1. P. 329.

128. *Gilbert A., Cameron A. G. W.* // Can. J. Phys. 1965. V. 43. P. 1446.

129. *Moretto L. G. et al.* // Phys. Lett. B. 1972. V. 38. P. 471.

130. *Karnaukhov V. A. et al.* // Phys. Rev. C. 2003. V. 67. P. 011601(R).

131. *Karnaukhov V. A. et al.* // Nucl. Phys. A. 2004. V. 734. P. 520.

132. *Ogul R., Botvina A. S.* // Phys. Rev. C. 2002. V. 66. P. 051601.

133. *Guarnera A.* // XXXIII Winter Meeting on Nucl. Phys., Bormio, 1995; Preprint GANIL P95-05. Caen, 1995.

134. *Lee S. J., Mekjian A. Z.* // Phys. Rev. C. 1997. V. 56. P. 2621.

135. *Baran V. et al.* // Nucl. Phys. A. 1998. V. 632. P. 287.
136. *D'Agostino M. et al.* // Phys Lett. B. 2000. V. 473. P. 219.
137. *Norbeck E. et al.* // Nucl. Phys. A. 1996. V. 607. P. 105.
138. *Beaulieu L. et al.* // Phys. Rev. C. 2002. V. 64. P. 064604.
139. *Natowitz J. et al.* // Ibid. V. 65. P. 034618.
140. *Moretto L. G. et al.* // Ibid. V. 66. P. 041601(R).
141. *Rivet M. F. et al.* // Nucl. Phys. A. 2005. V. 749. P. 73c.
142. *Chomaz P., Gulminelli F.* // Ibid. P. 3c.
143. *Pichon M. et al.* // Ibid. P. 93c.
144. *Gross D. H. E.* // Nucl. Phys. A. 1993. V. 553. P. 175c.
145. *Jaqaman H. R., Gross D. H. E.* // Nucl. Phys. A. 1991. V. 524. P. 321.
146. *Bugaev K. A. et al.* // Phys. Rev. C. 2000. V. 62. P. 044320.
147. *Greiner W., Stöcker H.* // Pour la Science. March 1985.
148. *Migdal A. B.* // J. Exp. Theor. Phys. 1971. V. 61. P. 2209; Rev. Mod. Phys. 1978. V. 50. P. 107.
149. *Weise W., Brown G.* // Phys. Lett. B. 1975. V. 58. P. 300.
150. *Lee T. T.* // Rev. Mod. Phys. 1975. V. 47. P. 267.
151. *Avdeyev S. P. et al.* // Nucl. Phys. A. 1982. V. 381. P. 419.
152. *Nagamia S.* // Nucl. Phys. A. 1988. V. 488. P. 3c.
153. *Ricatti L.* // Nucl. Phys. A. 2004. V. 734. P. 28c.
154. *Botvina A. S., Mishustin I. N.* // Phys. Lett. B. 2004. V. 584. P. 233.
155. *Margueron J. et al.* // Phys. Rev. C. 2004. V. 70. P. 02801.